



Supplementary Materials for

Broadband electro-optic polarization conversion with atomically thin black phosphorus

Souvik Biswas *et al.*

Corresponding author: Harry A. Atwater, haa@caltech.edu

Science **374**, 448 (2021)
DOI: 10.1126/science.abj7053

The PDF file includes:

Materials and Methods
Supplementary Text
Figs. S1 to S36
References

Other Supplementary Material for this manuscript includes the following:

Movies S1 to S4

Materials and Methods

S1. Fabrication process

Mechanically exfoliated tri-layers of BP (exfoliated using Scotch-tape) were identified on PDMS substrates with the aid of optical contrast. Mild heating of the tapes ($\sim 50\text{-}70^\circ\text{C}$) during the exfoliation process yields large area BP thin flakes. We found $\sim 7\%$ contrast in the grey channel per monolayer, meaning tri-layers showed around 21% contrast. This was also verified with optical absorption measurements for 1-5 layers of BP, where the bandgap changes dramatically with thickness. hBN and few-layer graphene (FLG) flakes were exfoliated (using Scotch-tape) on pre-cleaned SiO_2/Si chips (sonicated for 30 minutes in Acetone and Isopropanol (IPA), followed by oxygen plasma : 70 W, 90 mTorr for 5 minutes). Clean flakes of desired thickness ranges were identified with a combination of optical microscopy and atomic force measurements (AFM). A dome-shaped (polycarbonate/polydimethylsiloxane) PC/PDMS stamp was used to pick-up the individual layers in a top-down approach (hBN-BP-FLG-hBN), at temperatures between $70\text{-}110^\circ\text{C}$. Pre-patterned electrodes with back reflectors were prepared using electron-beam lithography (100 keV, 5nA) and electron-beam evaporation of Ti(3nm)/Au(100nm). Assembled heterostructures were dropped on the electrodes at 200°C . Subsequently, the PC film was washed by rinsing the sample overnight in chloroform and finally in IPA. For devices without the top mirror, this was followed by wire-bonding to chip carriers. For passive cavity samples, PMMA of desired thickness (adopted from calibration curve by Kayakuam) was spin-coated on the entire device, followed by baking at 180°C for 3 minutes. This was followed by electron-beam evaporation of the top metal (Au) of the desired thickness at $1\text{\AA}/\text{s}$ at base pressures of $\sim 3 \times 10^{-8}$ Torr. For active devices, this was followed by opening windows to the electrical contacts and wire-bonding to chip carriers.

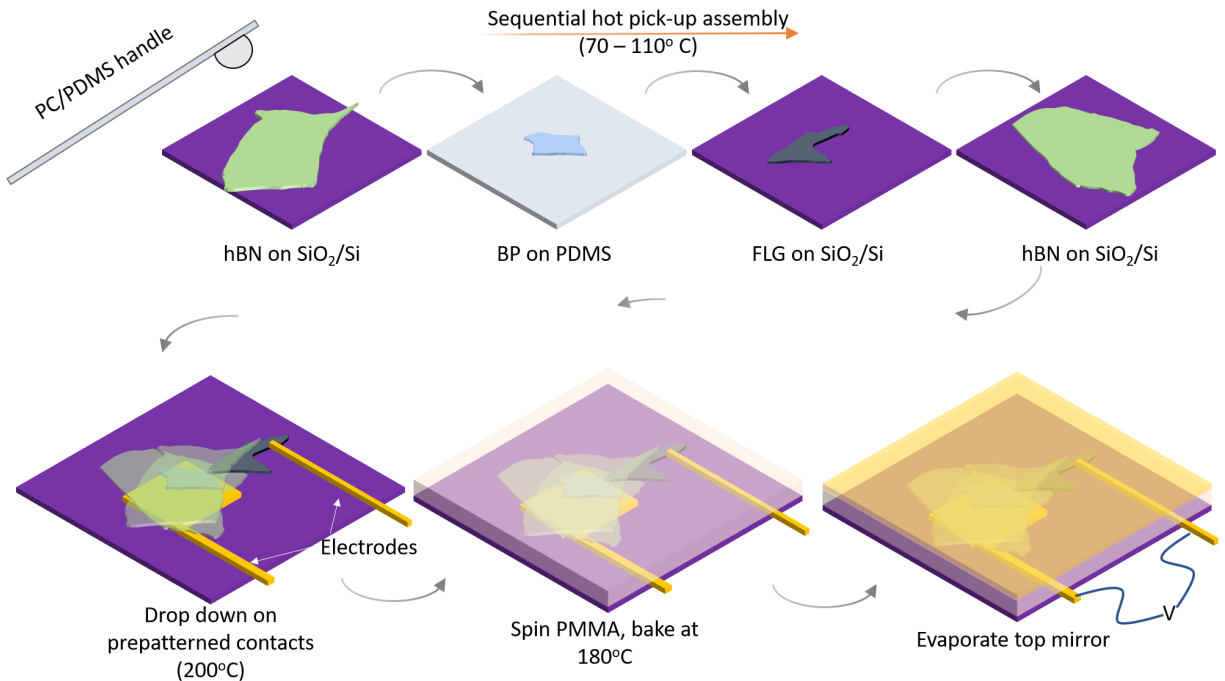


Figure S1. Schematic of the fabrication process illustrating the pickup process.

S2. Example of a typical BP staircase flake

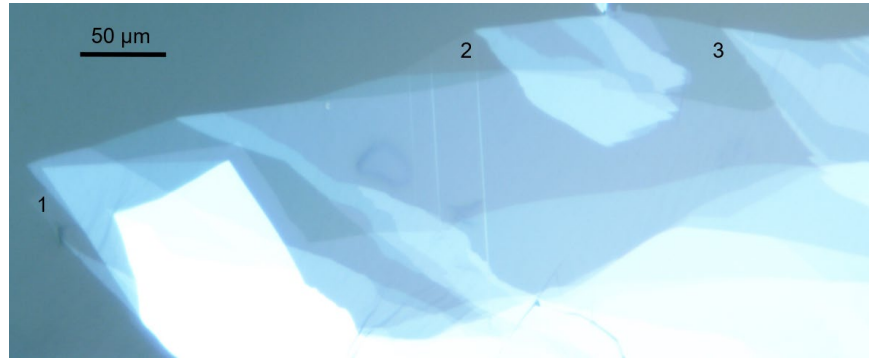


Figure S2. Optical image of a BP flake. A typical exfoliated BP staircase flake on PDMS. 1,2 and 3 layers are marked – confirmed with optical contrast. Other thicknesses can also be seen. Scale bar corresponds to 50 μm.

S3. Optical images of devices studied for this study

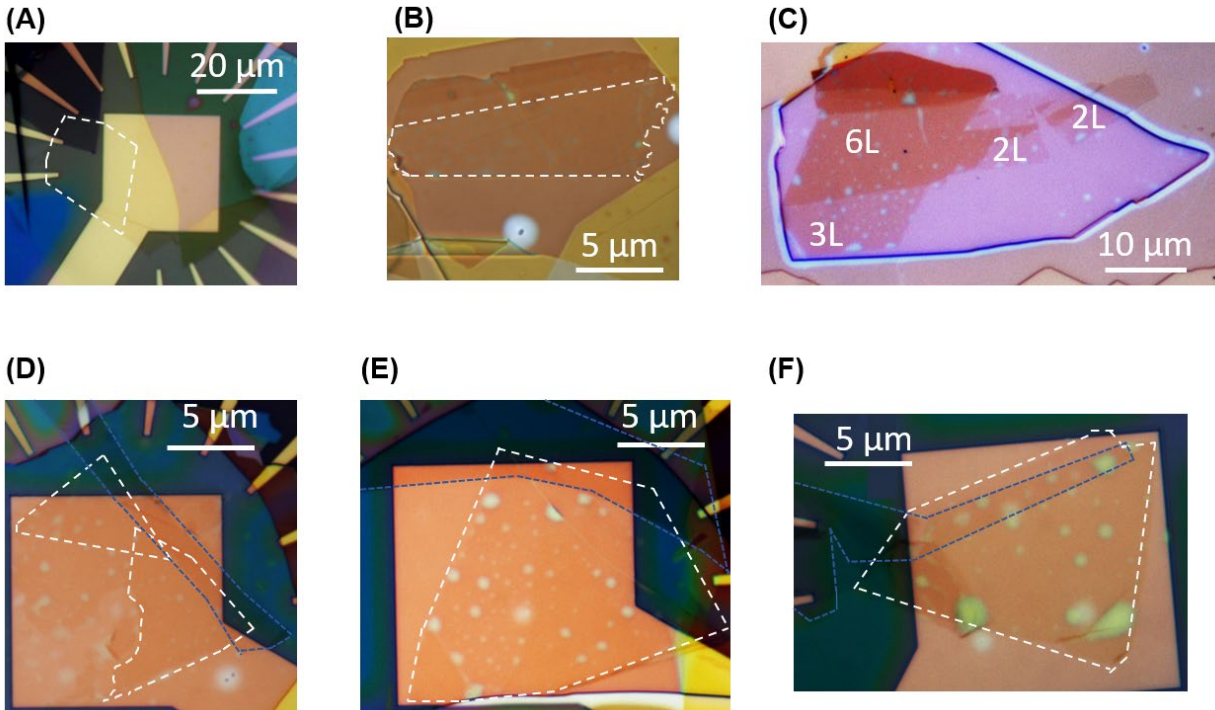


Figure S3. Optical images of representative devices investigated for this study. (A) – Non-cavity device for extracting electrically tunable complex refractive index of TLBP (shown in Fig. 2). (B), (C) – Passive cavity integrated devices. Spatial maps of (B) are shown in Fig. S17 and S18 and corresponds to D2. (C) shows D4, results of which are summarized in Fig. 3. (D), (E), (F) – Active cavity integrated devices. (D) shows D1, results of which are discussed in Fig. 4. (E) represents D5. Results from (F) are not discussed in this paper. The white outlines denote BP, while the blue outlines denote the contacting few layers graphene flake.

S4. Raman spectroscopy to identify BP crystal axes

Typical Raman spectra are shown as a function of the incident polarization (linear) of the excitation laser. The strongest response in the A_g^2 peak is seen for the armchair (AC) orientation, whereas for the zigzag (ZZ) orientation the same response is the weakest. This combined with linearly polarized absorption measurements enable robust determination of the BP crystal axes. A 514 nm laser was used for the excitation.

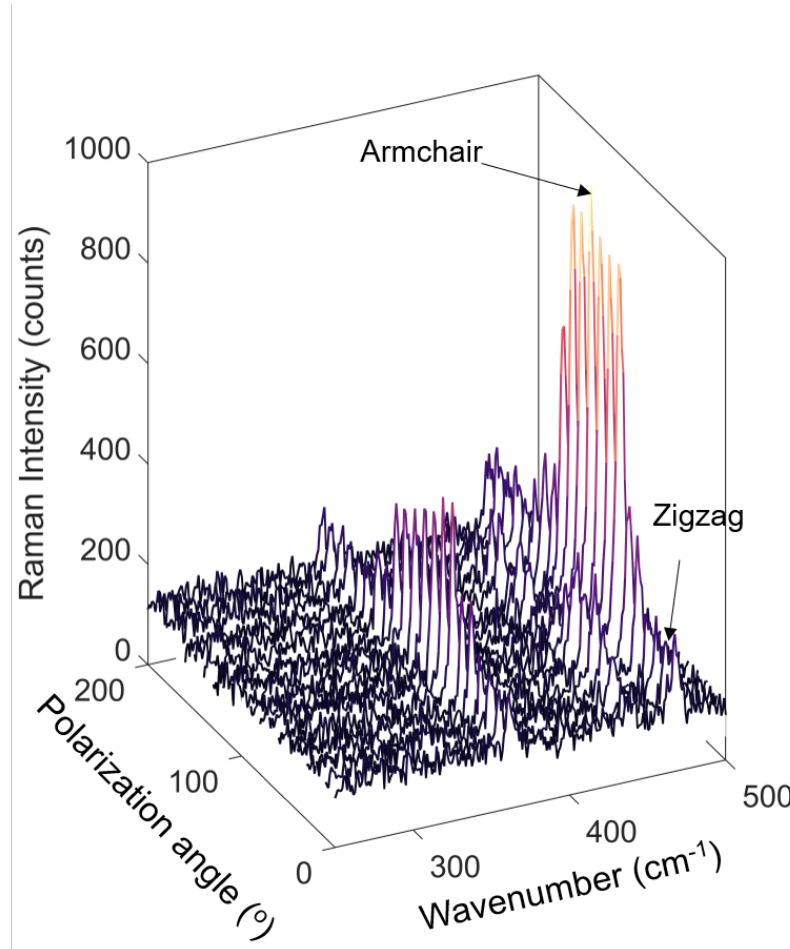


Figure S4. Polarized Raman spectroscopy for BP axis identification. Raman spectrum for TLBP as a function of incident linear polarization excitation. A_g^1 , B_{2g} and A_g^2 modes are seen clearly. Strongest response from the A_g^2 mode is seen along the armchair (AC) orientation, whereas along the zigzag (ZZ) direction it is the weakest.

S5. Charge density calculator

In the devices investigated in this work, the voltage was applied between the back-electrode/back-Au mirror and the TLBP (grounded). The charge accumulated in the TLBP was estimated using a parallel-plate capacitor model. Since the thickness of the TLBP samples studied (~ 1.6 nm) are below the Thomas-Fermi screening length (~ 3 nm) for charge densities accessed in this work ($< 10^{13}/\text{cm}^2$), the entire TLBP can be assumed to be equipotential. The bottom hBN is the dielectric capacitor, which enables the formation of a two-dimensional electron gas at the TLBP. Hence, the capacitance is calculated as follows :

$$C = \frac{\epsilon_0 \epsilon_r A}{d}$$

where, C = capacitance, ϵ_0 = vacuum permittivity, ϵ_r = relative dielectric permittivity of hBN ($\epsilon_r = 3.9$), A = area of the capacitor, d = thickness of the hBN flake.

The charge density is subsequently calculated as:

$$n = \frac{C}{A} (V - V_{\text{CNP}})$$

where, n = induced charge density (cm^{-2}), V = applied voltage, V_{CNP} = voltage at charge neutral point. The CNP is estimated from reflectivity measurements, where the highest excitonic absorption is seen. An example gate voltage to charge density (for device D1) conversion is shown.

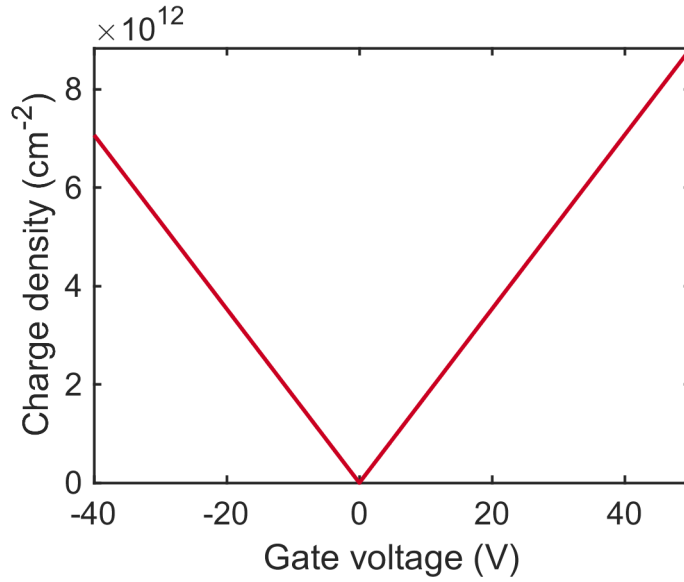


Figure S5. Parallel-plate capacitor model. Estimated charge density versus applied gate voltage for Device D1, using the parallel plate capacitor model.

S6. Schematic of the experimental setups used for optical characterization

The differential reflectivity measurements were done with the aid of a chopped (mechanical chopper ~419 Hz) supercontinuum white light source (Fianium Super-K FIU 15) and Ge photodetector. Input light was polarized with a wire-grid linear polarizer. Lock-in amplifiers were used to improve the overall signal quality, locked to the chopper frequency. Voltage was applied using Keithley 2400. In all measurements, the BP was grounded while voltage was applied to the back-electrode. A flat Au surface was used to normalize the reflectivity data. Newport motion controllers (ESP 301) were used to generate spatial maps.

For the polarization conversion measurements, a tunable laser in the near-infrared (Santec TSL-210 covering 1410 to 1520 nm and Newport Velocity 6400 covering 1500 to 1575 nm) was used as the source. A polarimeter (PAX1000IR2) was used to measure the polarization state of the reflected light. Motion controllers (MT3-Z8) were used to perform spatial mapping. Keithley 2400 was used to apply voltage. The input polarization state was controlled using a linear polarizer and a half-wave plate. Labview and python scripts were written to automate data acquisition.

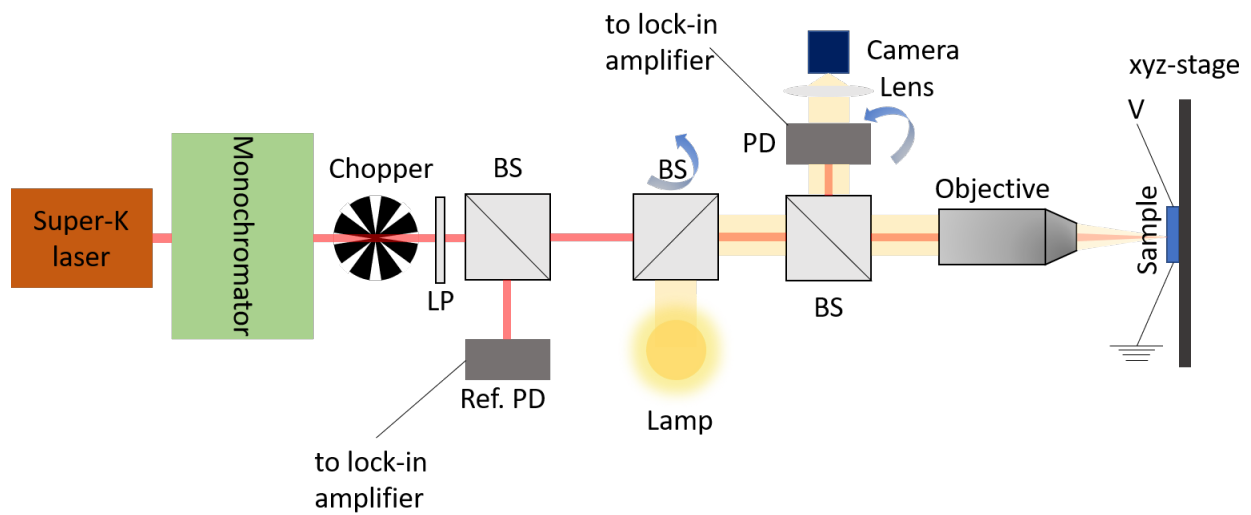


Figure S6. Broadband reflectivity characterization setup. Schematic of the optical setup used to characterize the complex refractive index of TLBP as a function of doping density. LP – linear polarizer (wire-grid), PD – photodetector (Ge), Ref. PD – Reference photodetector (Ge), BS – Beam splitter. Blue arrows denote optics on flip mounts.

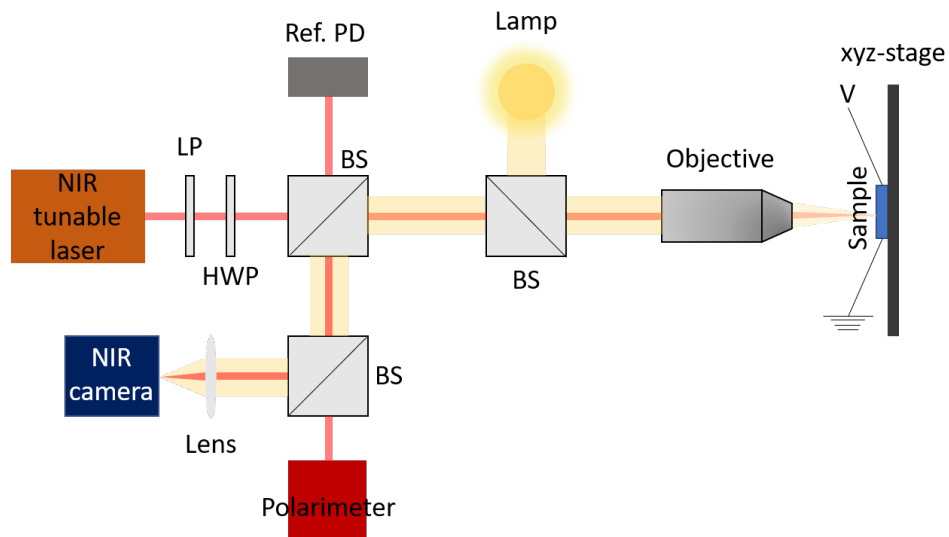


Figure S7. Polarization conversion measurement setup. Schematic of the optical setup used to characterize the polarization conversion. LP – linear polarizer, HWP – halfwave plate, Ref. PD – Reference photodetector (InGaAs), BS – Beam splitter.

Supplementary text

S7. Phenomenological tight-binding model for TLBP bandgap

We begin our discussion of the optical properties of TLBP with a simple phenomenological tight-binding model. TLBP is a direct bandgap semiconductor with its band minima at the Γ -point. In the low energy approximation, coupling among only nearest-neighbours needs to be considered. For monolayer BP, the Schrödinger equation reads:

$$H_{1k}\psi_{1k} = E_{1k}\psi_{1k}$$

H_{1k} is the Hamiltonian at the Γ -point for monolayer BP. For N-layers, considering nearest layer coupling as γ_k , the Hamiltonian can be constructed as:

$$H_{Nk} = \begin{pmatrix} H_{1k} & \gamma_k & 0 & \cdots & 0 \\ \gamma_k & H_{1k} & \gamma_k & \cdots & 0 \\ 0 & \gamma_k & H_{1k} & \cdots & 0 \\ \vdots & \vdots & \vdots & \ddots & \vdots \\ 0 & 0 & 0 & \cdots & H_{1k} \end{pmatrix}$$

Solving the N-layer Hamiltonian produces eigenvalues of the following form –

$$E_{Nk} = E_{1k} - 2\gamma_k \cos\left(\frac{n\pi}{N+1}\right), \text{ where } n=1, 2, 3 \dots N.$$

The optical transition energies are given by : $E_{ij}^N = E_{CB} - E_{VB} = E_{g0} - 2(\gamma_{CB} - \gamma_{VB})\cos\left(\frac{n\pi}{N+1}\right)$, where $E_{g0} = E_{CB1} - E_{VB1}$ is the bandgap of monolayer BP. For 3 – layers, using $E_{g0} = 1.9$ eV, $\gamma_{CB} - \gamma_{VB} = 0.73$ eV, (known from previous studies ((24, 25, 28))) we achieve $E_{11}^3 = 0.868$ eV = 1429 nm, which is in close agreement with the measured optical bandgap of 1398 nm. Thus, the tight binding model works as a good approximation to estimate the lowest energy optical transition for TLBP.

S8. Discussion of anisotropy and electro-optic response in BP

At the Γ -point of the band-structure in BP, wave functions are either even or odd with respect to reflection across reflection plane σ_h which lies in the x-z plane (where, x is AC, and z is out-of-plane axis) (25). Wave functions along the x (AC) direction are even with respect to σ_h , whereas those along the y (ZZ) direction are odd. This implies that in a $\mathbf{k}\cdot\mathbf{p}$ approximation, the perturbing Hamiltonian contains vanishing linear terms in the y-direction and close to the Γ -point, the system becomes quasi-one- dimensional. This induces a rather strong anisotropy, especially pronounced at the excitonic resonance/optical band-edge due to the higher optical density of states and the system behaves like an ensemble of one-dimensional exciton chains along the x-direction. In the absence of excitonic features in TLBP, in the near infrared, the dielectric permittivities for the AC and ZZ directions are set by the higher energy oscillators ($\epsilon_\infty = 12.5$ (AC), 10.2 (ZZ)), which because of differences in the crystal symmetry along those two directions, gives rise to a broadband anisotropy. This anisotropy is exaggerated due to an excitonic feature in the telecom band for TLBP.

Having established the anisotropy in BP, we move on to explain the strong electrical tunability of the optical properties of BP. When the system (BP) is near charge-neutral/flat-band conditions, the optical susceptibility is strongly dominated by the neutral exciton resonance – which is manifested as a strong peak in absorption along the AC direction. As the gate voltage is tuned to positive/negative values, a two-dimensional electron gas (2DEG) forms at the interface of BP and the bottom hBN. This 2DEG, which effectively increases the Fermi level of BP, results in the following changes:

Coulomb screening of the exciton – This is the predominant mechanism of modulation in our current scheme of electrostatic gating. As the charge density in the 2DEG in TLBP increases, the free carriers effectively screen the field between the bound electron-hole pairs. This reduces the interaction strength of the quasi-one-dimensional dipoles in TLBP (along the AC direction), increases its Bohr radius, and leads to a reduction in the exciton binding energy and thus lowers the oscillator strength. This mechanism is thus also responsible for tuning the anisotropy in the system with gate voltage, as it effectively diminishes the excitonic contribution and the difference of optical response along the AC and ZZ direction are eventually dictated by the higher energy oscillators (ϵ_∞).

Coulomb scattering of the exciton – This is another important consequence of gating. With more free carriers available, the probability of an exciton to elastically or inelastically scatter off an electron or hole increases. This leads to a reduction in coherence lifetime of the exciton which manifests itself as spectral broadening corresponding to the excitonic transition, seen for both electron and hole doping in our case.

The combined effects are schematically illustrated in Fig. S8.

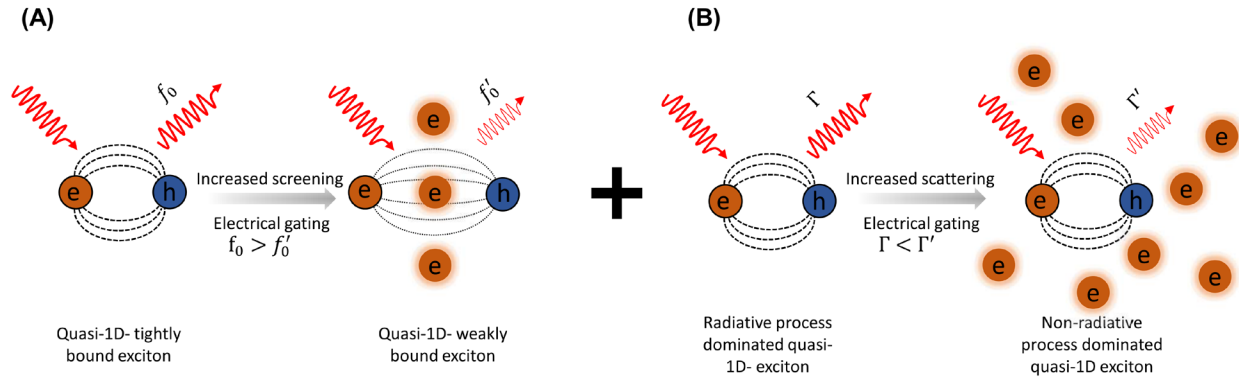


Figure S8. Coulomb screening and scattering of quasi-1D excitons. (A) Due to electrical gating, free charges increase which reduce the overall attraction between the bound electron-hole pair for the quasi-1D excitons along the AC direction. This screens the electric field lines between them and weakens the exciton, leading to a reduction in binding energy and oscillator strength (f_0). (B) Due to increased charges, excitons now scatter off them much more readily, leading to reduced coherence and broadening of spectral transitions, manifested as larger linewidths (Γ).

We also address some other electro-optic effects seen in typical 2D semiconductors that might be at play:

- **Trions** – As excess free electrons/holes accumulate in the 2DEG, the probability of an exciton to bind to a free charge to form a trion increases. Compared to the exciton, a trion is lower in energy which manifests as a redshift of the absorption peak. Generally, trions have lower oscillator strength compared to excitons and hence can show up as a reduced absorption peak. This explains the redshift of the excitonic peak upon hole doping (which happens to be more efficient than electron doping for the investigated non-cavity device).
- **Band-structure (gap) renormalization** – In the presence of excess free carriers, there can be significant band-structure renormalization which leads to energy shifts in the absorption peak. Typically, band-gap renormalization red shifts the quasiparticle gap. A near exact cancellation of this effect is expected from the reduction in the binding energy of the exciton leaving the spectral position of the exciton nearly unchanged for the doping densities achieved here. This phenomenon is not probed directly through our measurements since the quasi-particle gap is not tracked.

- Pauli blocking – As the Fermi level is increased, the lowest optical transitions below the Fermi level get blocked because of Pauli’s exclusion principle, resulting in a blue-shift of the absorption peak. Such features were not seen in our measurements and are expected to occur at much higher charge densities ($>10^{13}/\text{cm}^2$).
- Stark shift – The 2DEG induced in BP has its own vertical electric field which can cause a reduction of the bandgap and a red-shift of the absorption peak. We believe this is a very weak (and thus negligible) effect in our current scheme of electrostatics where a pure vertical displacement field (in absence of doping) does not exist, rather the vertical field arises from a thickness dependent doping profile, due to screening. Since the entire thickness of TLBP is below the Thomas-Fermi screening length (see S28), it is justified to consider the entire film to be under uniform doping and have minimal displacement field-dependent energy shifts.

The above-listed 4 effects play a minor role and the most significant effect responsible for large polarization conversion in the cavity-based devices is a change in the oscillator strength of the exciton, as seen later in S20.

The overall effect of the electrostatic doping on the quasi-1D excitonic absorption spectrum can be schematically represented as follows:

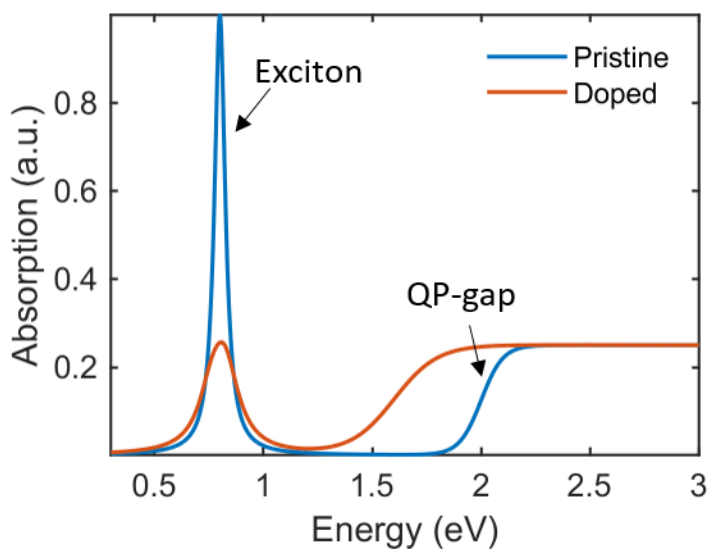


Figure S9. Absorption modulation schematic upon doping. Illustrated modulation in absorption reflecting changes in the optical density of states upon doping showing a reduction of exciton oscillator strength and broadening of the transition along with bandgap renormalization and reduction of quasi-particle (QP) band-edge coupled with a reduction in exciton binding energy rendering the exciton resonance nearly unchanged spectrally.

S9. Discussion about the excitonic framework in TLBP and doping dependence

While the 1-D tight binding model works as a good approximation to estimate the optical bandgap (and higher order transitions) of TLBP, it is not sufficient to capture the screening effects which dictate the optical susceptibility of the system at finite-doping levels, since it does not capture the electron-hole correlations. A more accurate way to model the susceptibility of TLBP is to consider excitons in the Wannier-Mott framework, where they obey the following equation –

$$\left(-\frac{\delta}{\mu_x^* \delta x^2} - \frac{\delta}{\mu_y^* \delta y^2} + V_{eh}(r) \right) \psi_i(x, y) = E_i \psi_i(x, y)$$

where, $\mu_{x/y} = \left(\frac{1}{m_{e_{x/y}}^*} + \frac{1}{m_{h_{x/y}}^*} \right)^{-1}$ is the reduced excitonic mass of TLBP in the AC (x) and ZZ (y) direction, and m_e^* and m_h^* represent the conduction and valence band effective masses. It is noteworthy that the optical transitions in the ZZ direction remain disallowed due to symmetry arguments (see S8).

Taking into account the polarizability of the 2D-sheet and nonlocal screening from the environment, the e-h interaction potential can be simplified into the Rytova-Keldysh potential as follows:

$$V_{eh}(r) = -\frac{2\pi e^2}{(\epsilon_a + \epsilon_b)r_0} \left[H_0\left(\frac{r}{r_0}\right) - Y_0\left(\frac{r}{r_0}\right) \right]$$

where, $r = \sqrt{x^2 + y^2}$ is the e-h distance, H_0 and Y_0 are the Struve and Neumann functions, respectively. ϵ_a and ϵ_b are the dielectric function of the environment (in our case, hBN, $\epsilon_{hBN} = 3.9$) and $r_0 = \frac{d\epsilon_{TLBP}}{\epsilon_a + \epsilon_b}$ is the screening length, with d = thickness of TLBP (1.59 nm) and ϵ_{TLBP} is the dielectric function of TLBP. The screening length (all other parameters kept constant) primarily depends on the dielectric function (ϵ_{TLBP}) or the polarizability of the TLBP. Under static conditions (no doping), the aforementioned set of equations can be solved numerically to obtain the binding energies of the entire Rydberg series of excitons along the AC direction. It is noteworthy, that within our window of optical measurements, only the ground state of the Rydberg series is experimentally probed. Under finite doping, the polarizability or the dielectric function of TLBP is heavily modified since the excitonic contribution is suppressed due to a decrease of the screening length (r_0) – realized from Thomas-Fermi screening calculations. Assuming $m_{eff} = 0.16m_0$, we numerically solve for the binding energy of the ground state exciton as a function of the screening length (r_0). The range of screening lengths is extracted from Thomas-Fermi calculations of band-bending, which for the range of doping densities accessed in these measurements ($n = 10^{12}/\text{cm}^2$ to $7 \times 10^{12}/\text{cm}^2$) turns out to be approximately between 2 and 10 nm, decreasing with increasing charge density. It can be clearly seen that the binding energy drops with the reduction in screening length, in line with our measurements. Note that the Hamiltonian is only solved along the AC direction.

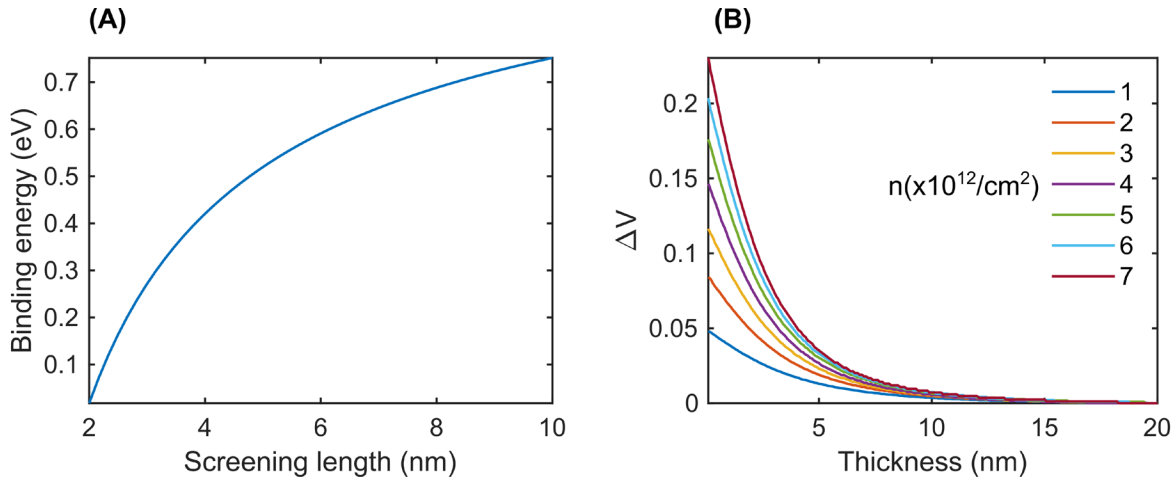


Figure S10. Binding energy change with screening length and doping. (A) Calculated binding energy of the ground state exciton as a function of screening length using the Rytova-Keldysh potential. (B) Band-bending (screening profile) as a function of doping density in BP.

Furthermore, the oscillator strength of the excitonic absorption varies inversely with the Bohr-radius of the exciton, $|\phi_{ex}(n)|^2 \propto 1/a_B^2(n)$. In the presence of finite doping with a reduction in the binding energy, the Bohr-radius increases, leading to a drop in the oscillator strength.

S10. Extracted exciton parameters for TLBP as a function of gate voltage/doping density:

Having discussed a theoretical framework for the modulation mechanism, we present here the results of the different exciton parameters (modelled as a Lorentzian) as a function of doping density, which enables us to quantify the doping dependence. The optical sheet conductivity of TLBP is modelled as follows :

$$\tilde{\sigma}(\omega) = \frac{4i\sigma_0 f_0 \omega}{\omega - \omega_0 + i\Gamma/2}$$

where, σ_0 is the universal conductivity, ω_0 = exciton frequency/resonance wavelength, f_0 = oscillator strength and Γ = broadening/linewidth of the resonance.

The optical conductivity can be converted to complex refractive index via the following relations:

$$\tilde{\epsilon} = \epsilon_\infty + \frac{i\tilde{\sigma}(\omega)}{d_{BP}\epsilon_0\omega}$$

$$\tilde{n} = n + ik = \sqrt{\tilde{\epsilon}}$$

where, ϵ_∞ accounts for the contribution of higher (than the exciton) energy resonances, d_{BP} = thickness of the BP layer and $\tilde{\epsilon}$ and \tilde{n} are the complex dielectric function and refractive index.

By fitting the gate dependent differential reflectivity measurements (Fig 1B) using transfer matrix calculations, we extracted the exciton parameters at each voltage. Fig. S11A tracks the changes in the resonance wavelength corresponding to the excitonic transition. A strong redshift is seen for negative gate voltages (hole doping), whereas very mild blueshift is seen for positive gate voltages (electron doping). An inset shows the relationship between the applied gate voltage and estimated charge density using the capacitor model discussed in S5. On either sides of charge neutral condition (0V), a reduction of the oscillator strength is seen (more dramatic on the hole side) with a broadening of the resonances, summarized in Fig. S11B and S11C, respectively. These observations are in line with the expected electro-optic effects – the strong Coulomb screening from the excess induced carriers reduces the binding energy of the exciton and lowers its oscillator strength. Increased scattering of the excitons with free charges increases the effective linewidth of the transition. The asymmetry between the electron and hole doping is likely related to the efficiency of contacts to BP and the presence of defect states that pin the Fermi energy on the electron side, thus limiting the modulation depth. This also explains why for hole doping a redshift is seen – due to higher gating efficiency the optical response is dominated by trions which are at lower energies than excitons, whereas for the electron side the contribution is comparatively less. We note that at room temperature, optical features are quite broad in BP and since no explicit trion peak was observed, the absorption was modelled with a single Lorentzian feature corresponding to the exciton.

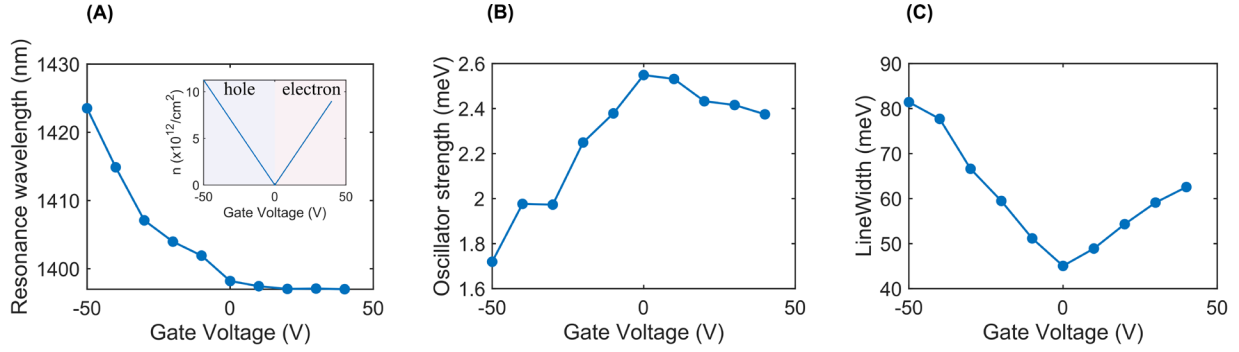


Figure S11. Exciton parameter modulation with gate voltage for TLBP. Tuning of the exciton resonance parameters as a function of applied gate voltage. (A), (B) and (C) show changes in the resonance wavelength, oscillator strength and the linewidth of the excitonic resonance as a function of gate voltage, respectively. An inset in (A) shows the relation between the applied gate voltage and the estimated charge density in the BP 2DEG.

S11. Variation of the integrated optical conductivity (loss function) with doping

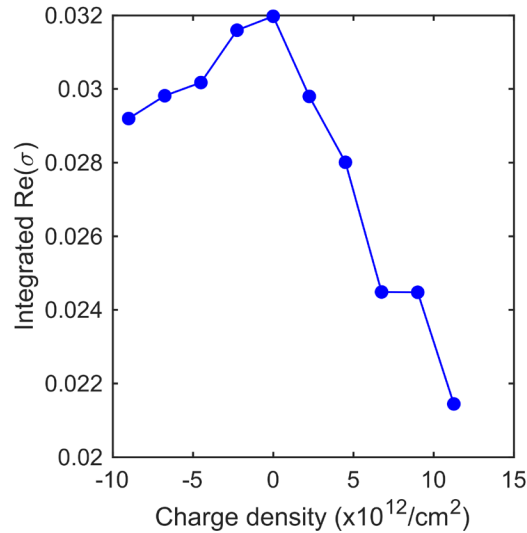


Figure S12. Integrated real optical conductivity variation with doping. The real part of optical conductivity is proportional to the loss function ($\propto \text{Im}(\epsilon)$) which dictates the overall optical response for such thin films. As doping is increased on either side, a drop in the loss function indicates reduced absorption due to screening of the excitons via free charges leading to a reduction in binding energy and oscillator strength. The integration (over optical measurements bandwidth) assumes a single excitonic feature and no other oscillators.

S12. Transfer matrix formalism for theoretical design of cavity-based devices

We employed a transfer matrix model to account for the multiple reflections in our cavity-based devices. It is formulated as follows –

For a stack consisting of N layers, we have

$$\begin{pmatrix} t \\ 0 \end{pmatrix} = M_{N_{\text{total}}} \begin{pmatrix} 1 \\ r \end{pmatrix}, \text{ where } M_{N_{\text{total}}} = \prod_{i=1}^N M_i(\omega)$$

$$M_i(\omega) = \frac{1}{2} \begin{pmatrix} e^{i(k_i - k_{i+1})z_i} \left(1 + \frac{k_i - \omega \mu_0 \sigma}{k_{i+1}}\right) & e^{-i(k_i + k_{i+1})z_i} \left(1 - \frac{k_i + \omega \mu_0 \sigma}{k_{i+1}}\right) \\ e^{i(k_i + k_{i+1})z_i} \left(1 - \frac{k_i - \omega \mu_0 \sigma}{k_{i+1}}\right) & e^{-i(k_i - k_{i+1})z_i} \left(1 + \frac{k_i + \omega \mu_0 \sigma}{k_{i+1}}\right) \end{pmatrix},$$

k = wavevector, z = thickness, i = layer index

The term $\omega \mu_0 \sigma$, where σ is the sheet conductivity, may be invoked only at interfaces containing 2D-thin films (for example, TLBP) where optical conductivity is used, else excluded if refractive index is used. Both approaches produced consistent results for non-cavity devices. However, for cavity-based devices refractive index approach was used due to its accuracy over the sheet conductivity model due to multiple round trips of light within the cavity (leading to increased “optical thickness” of thin 2D sheets). Reflection and transmission are given by:

$$T(\omega) = \frac{\tilde{n}_N}{\tilde{n}_1} |t|^2, \quad R(\omega) = |r|^2, \quad \text{where } \tilde{n}_m = \text{complex refractive index of layer } - m$$

S13. Jones matrix for TLBP birefringence and calculation of Stokes parameters

The polarization state of the reflected light from a device with TLBP can be calculated using the Jones vector method as follows. First, the reflected light amplitude and phase are calculated using the transfer matrix method assuming illumination along only the AC or the ZZ direction. Then, the cavity can be treated as a retarder plate (for both amplitude and phase) and its Jones matrix is given as:

$$J_{\text{cavity}} = \begin{pmatrix} r_{AC} e^{i\phi_{AC}} & 0 \\ 0 & r_{ZZ} e^{i\phi_{ZZ}} \end{pmatrix}$$

For a given rotation (θ) between the input optical beam and the TLBP axis, the effective Jones matrix is:

$$J_{\text{out}} = R(\theta) \begin{pmatrix} r_{AC} e^{i\phi_{AC}} & 0 \\ 0 & r_{ZZ} e^{i\phi_{ZZ}} \end{pmatrix} R(-\theta)$$

$$R(\theta) = \begin{pmatrix} \cos(\theta) & -\sin(\theta) \\ \sin(\theta) & \cos(\theta) \end{pmatrix}$$

$$J_{\text{out}} = \begin{pmatrix} \cos(\theta) & -\sin(\theta) \\ \sin(\theta) & \cos(\theta) \end{pmatrix} * \begin{pmatrix} r_{AC} e^{i\phi_{AC}} & 0 \\ 0 & r_{ZZ} e^{i\phi_{ZZ}} \end{pmatrix} * \begin{pmatrix} \cos(\theta) & \sin(\theta) \\ -\sin(\theta) & \cos(\theta) \end{pmatrix}$$

$$J_{\text{out}} = \begin{pmatrix} r_{AC} e^{i\phi_{AC}} \cos^2(\theta) + r_{ZZ} e^{i\phi_{ZZ}} \sin^2(\theta) & \cos(\theta) \sin(\theta) (r_{AC} e^{i\phi_{AC}} - r_{ZZ} e^{i\phi_{ZZ}}) \\ \cos(\theta) \sin(\theta) (r_{AC} e^{i\phi_{AC}} - r_{ZZ} e^{i\phi_{ZZ}}) & r_{AC} e^{i\phi_{AC}} \sin^2(\theta) + r_{ZZ} e^{i\phi_{ZZ}} \cos^2(\theta) \end{pmatrix}$$

Let $E_x = r_x e^{i\phi_x}$ and $E_y = r_y e^{i\phi_y}$, then, the Stokes parameters are given as:

$$S_0 = |E_x|^2 + |E_y|^2, S_1 = |E_x|^2 - |E_y|^2, S_2 = 2\text{Re}(E_x E_y^*), S_3 = -2\text{Im}(E_x E_y^*)$$

For clarity, the Stokes parameters can be normalized as:

$$s_1 = \frac{S_1}{S_0}, s_2 = \frac{S_2}{S_0}, s_3 = \frac{S_3}{S_0}$$

The azimuthal and ellipticity can then be calculated as:

$$\psi (\text{azi.}) = \arctan\left(\frac{s_2}{s_1}\right), \chi (\text{ell.}) = \arctan\left(\frac{s_3}{\sqrt{s_1^2 + s_2^2}}\right)$$

S14. Effect of PMMA and top mirror thickness on phase difference and cavity reflection

We present numerical results on the effect of the top Au and PMMA thickness on the cavity performance. Here, the thickness of the bottom Au, bottom hBN, TLBP and top hBN were fixed at 100 nm, 120 nm, 1.59 nm, and 52 nm. The refractive indices of Au were adopted from Johnson and Christy, while $n=2.17$ was used for hBN with no dispersion. For PMMA, $n=1.478$ was used. AC response of TLBP was modelled with a single exciton with the following parameters – resonance wavelength = 1398.2 nm, oscillator strength = 2.5 meV, broadening/linewidth = 45.1 meV (as extracted from measurements discussed in Fig 2.). $\epsilon_\infty = 12.5$ and 10.2 was used for the AC and ZZ direction, respectively. The ZZ direction permittivity was assumed to be constant, with no excitonic feature. No thickness dependence was assumed for the complex refractive index for any of the layers. Transfer matrix calculations were run with sweeps of the PMMA thickness and the top Au thickness. Fig. S15A shows the evolution of the cavity resonance. As the PMMA thickness is swept, the cavity resonance redshifts due to the overall increase in the optical length of the cavity. As the top Au thickness is increased, the resonance frequency blueshifts because of the change in the reflectivity of the top mirror (higher reflectivity for thicker top Au). Fig S15B shows the effect of the top Au and PMMA thickness on the reflection amplitude at the resonance along the AC direction. A trajectory is seen with low reflectivity highlighting the critical coupling condition. This is the physical set of parameters which correspond to the maximal energy transfer to the cavity. Finally, the maximum achieved phase shift difference between the AC and ZZ directions as a function of top Au and PMMA thickness is discussed in Fig. S15C. Strong phase difference is seen along the “critical coupling” trajectory. In this work, cavities were fabricated with target critical coupling to the AC direction because that is the electrically tunable polarization direction, while the ZZ remains passive for all doping conditions.

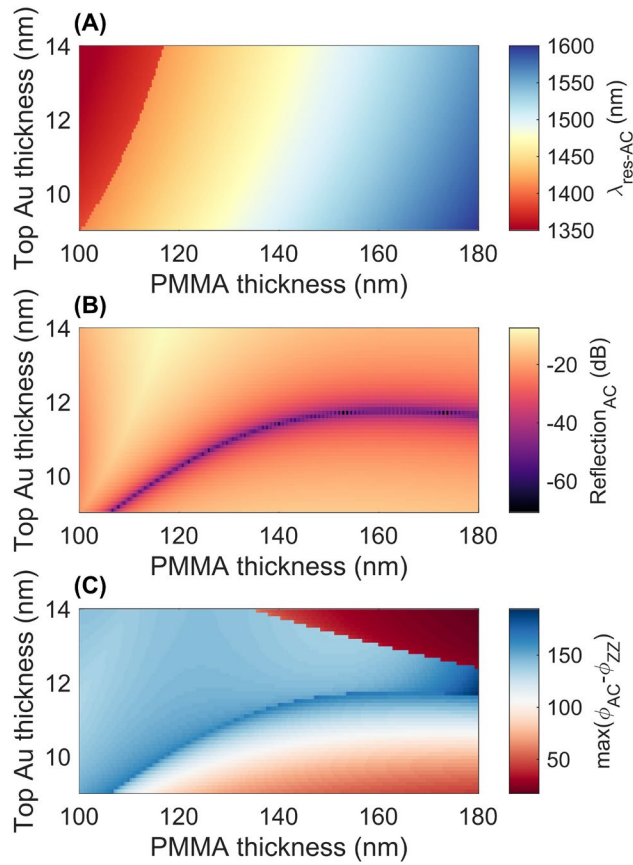


Figure S13. Amplitude and phase shift dependence on cavity parameters. Effect of the top Au and PMMA thickness are studied on the cavity performance. (A) Resonance of the cavity (along the AC direction) showing redshifts with increasing PMMA thickness and blueshifts with increasing metal thickness. (B) Reflection amplitude of the cavity (along the AC direction) showing the “critical coupling” trace as a function of top Au and PMMA thickness. (C) Maximum phase shift difference between the AC and ZZ direction plotted as a function of top Au and PMMA thickness. Strong phase shift difference traces follow the reflection amplitude trace, highlighting the importance of critical coupling.

S15. Broadband polarization conversion

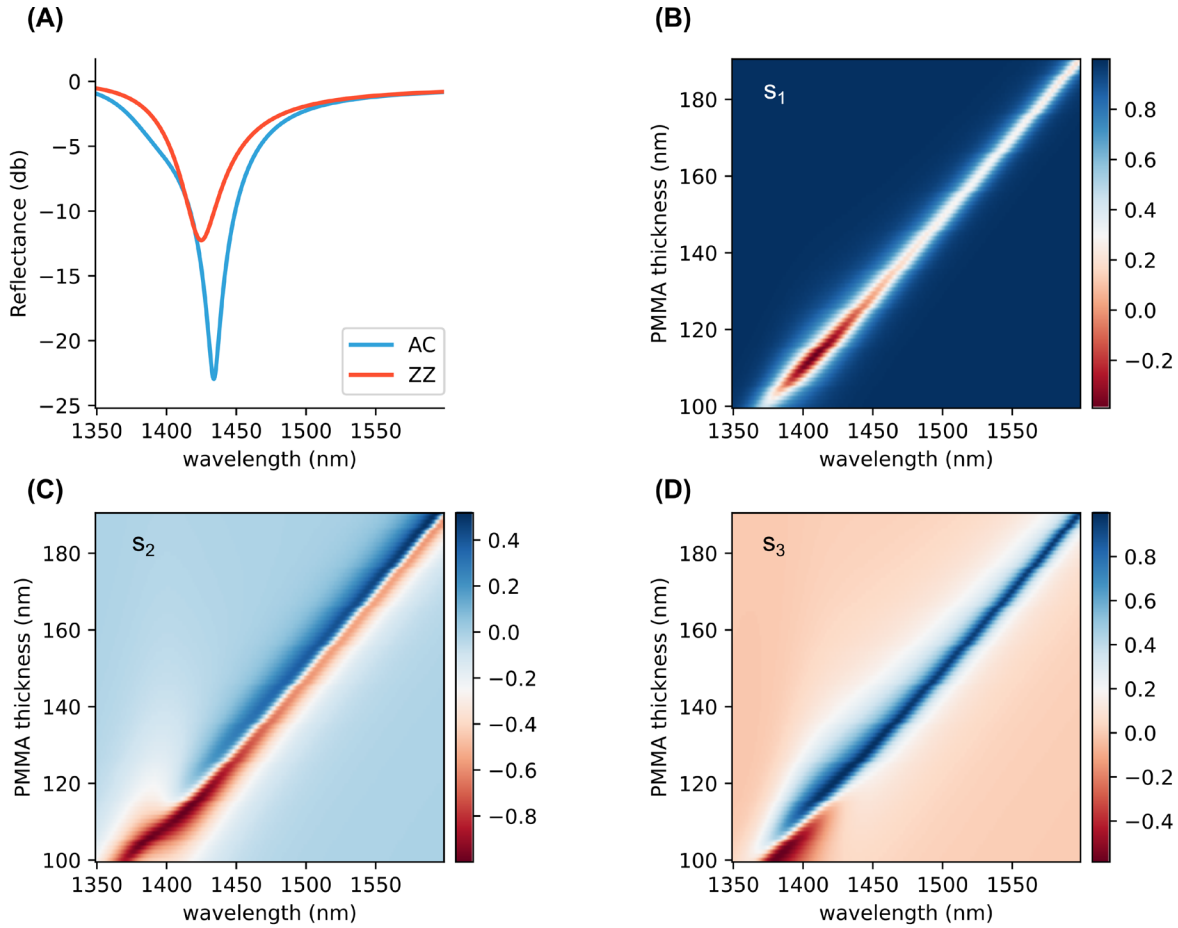


Figure S14. Broadband polarization conversion simulations. (A) Reflectance along the AC and ZZ direction for a cavity with parameters matching D1. (B), (C), (D) Normalized Stokes parameters (s_1 , s_2 , s_3) as a function of cavity length obtained by tuning the PMMA thickness showing efficient broadband polarization conversion.

S16. Spatial variation of refractive index in a non-cavity sample in TLBP

Results from a non-cavity device containing TLBP flake encapsulated in hBN on Au are presented here. Spatial variation of the complex refractive index is seen across the flake. The TLBP studied here was broader in linewidth.

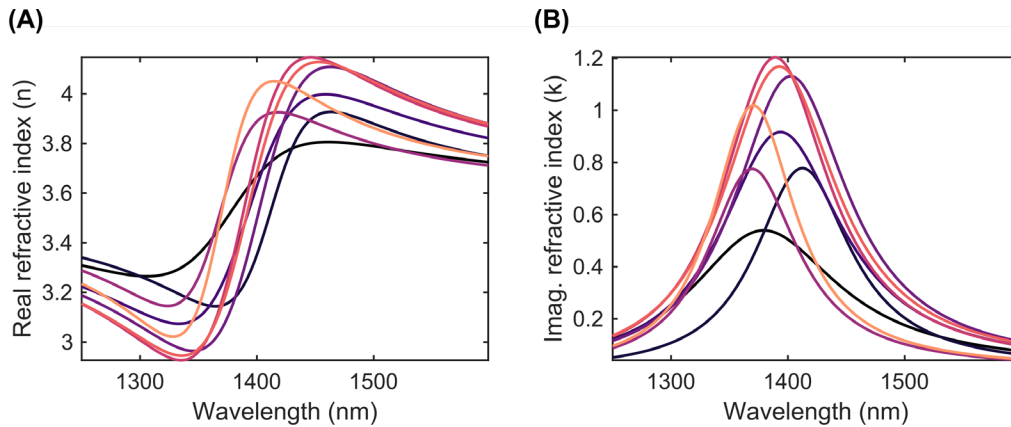


Figure S15. Spatial optical inhomogeneity in TLBP samples. Spatial variation of real (A) and imaginary (B) part of complex refractive index in a TLBP flake.

S17. Spatial maps in additional sample showing spatial non-uniformity

Spatial maps of ellipticity and azimuthal angles are presented for device D2 for different wavelengths. All maps show spatial inhomogeneity attributed to dielectric disorder that originates from strain or trapped bubbles during the heterostructure assembly of the device. Similar trends were observed in all the devices.

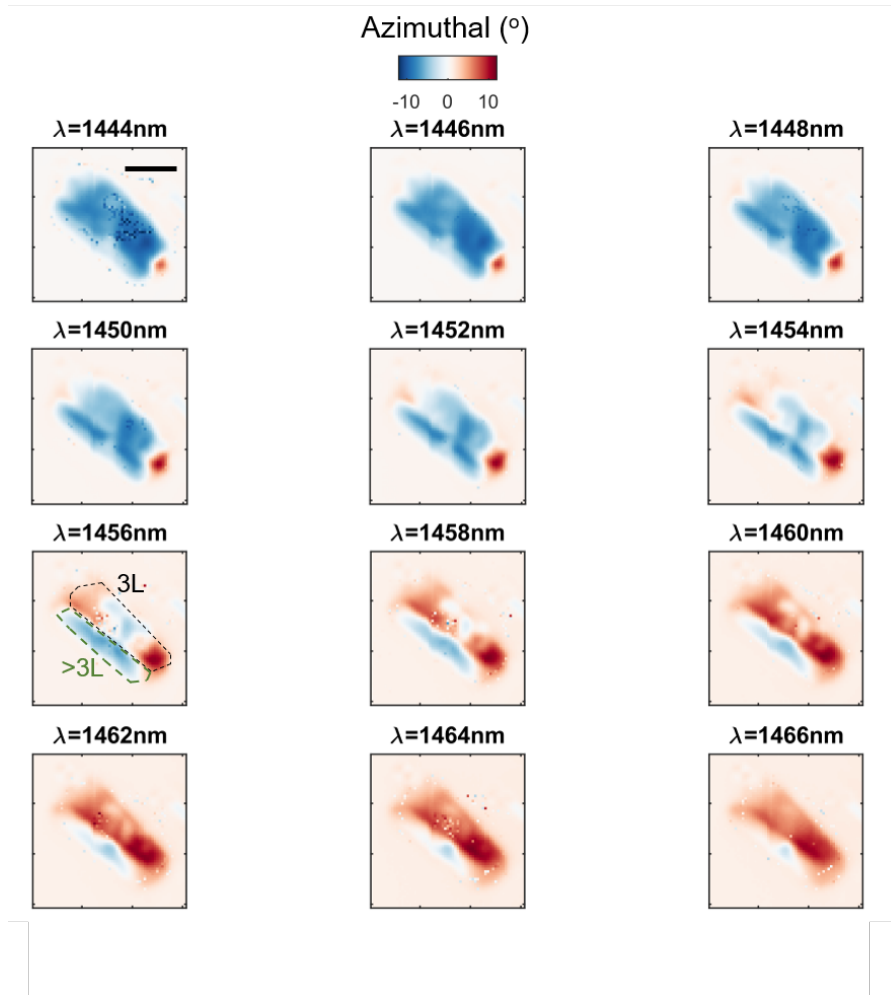


Figure S16. Azimuthal spatial colormaps of sample D2 for different wavelengths. Scale bar corresponds to 10 μm . 3L region is outlined in black dashed lines for 1456 nm spatial map, while thicker region is outlined in green.

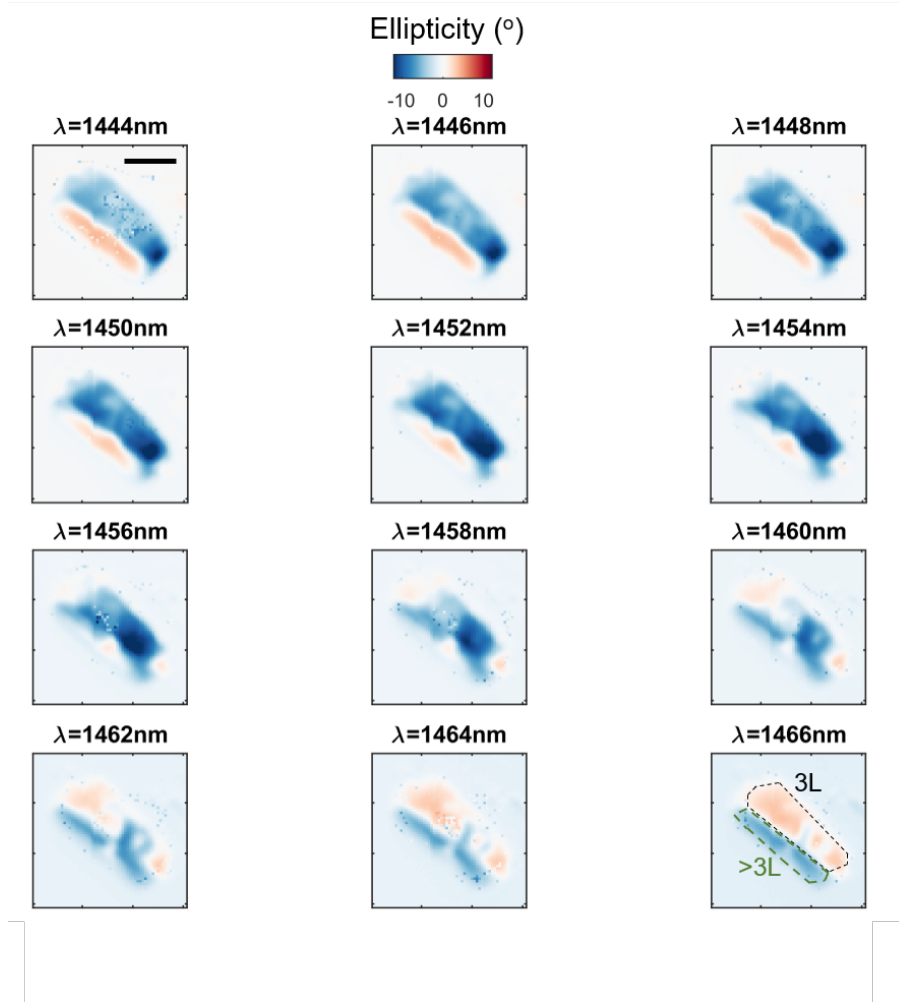


Figure S17. Ellipticity spatial colormaps of sample D2 for different wavelengths. Scale bar corresponds to 10 μm . 3L region is outlined in black dashed lines for 1466 nm spatial map, while thicker region is outlined in green.

S18. Effect of different thickness on the cavity resonance and polarization conversion

A staircase sample was fabricated to study the effect of different thicknesses of BP on the cavity resonance. A systematic red shift is seen as a function of BP thickness, as expected. Adding more layers increases the effective optical path length inside the cavity which explains the redshift of resonance. However, very weak polarization conversion was seen from thicknesses other than 3-layers. This reiterates the importance of choosing tri-layer flakes for working in the telecommunications band, since the anisotropy is very high near the excitonic resonance. In figure S19A, B, C reflection spatial colormaps can be seen at three different wavelengths (1460 nm, 1510 nm, and 1560 nm) showing changes in contrast for different thicknesses. Figure S19D illustrates the systematic redshift of the cavity resonance as a function of thickness. Figure S19E, F illustrates strongest polarization conversion in the 3L region as quantified by the ellipticity and azimuthal angle.

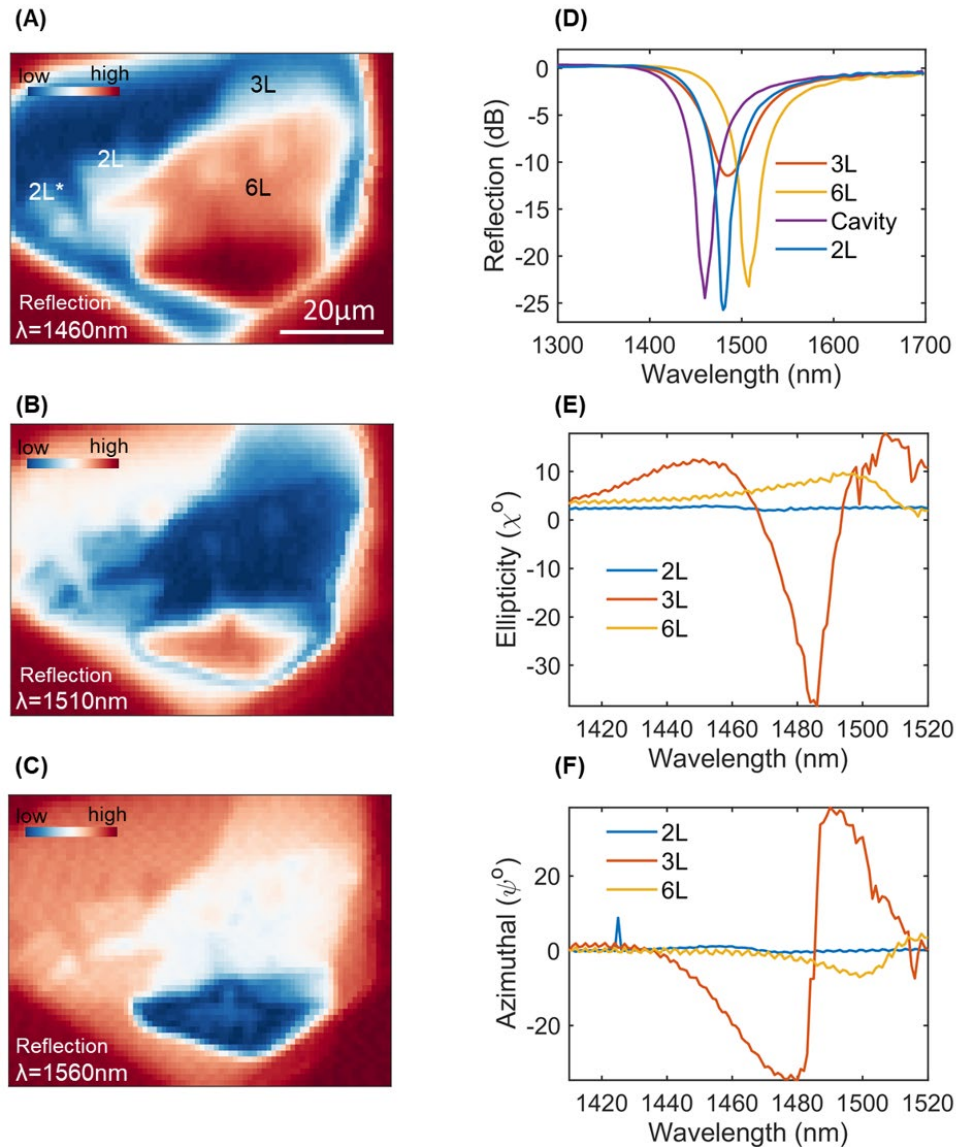


Figure S18. Effect of thickness on the cavity resonance and polarization conversion. (A), (B), (C) Reflection spatial maps at 3 different wavelengths (1460 nm, 1510 nm, and 1560 nm) for device D4 showing difference in contrast for different thicknesses of BP. (D) Reflection amplitude spectrum for different thicknesses of BP (2,3 and 6 layers) and bare cavity – illustrating redshift of cavity resonance with increasing thickness of BP. (E) Ellipticity and (F) Azimuthal angle spectrum for 3 different thicknesses of BP, showing highest polarization conversion in TLBP (3-layers).

S19. Effect of the incident polarization state on the polarization conversion

We investigate here, numerically, the effect of incident polarization on the spectral trajectory traversed on the normalized Poincaré sphere. To illustrate conditions close to the experimental measurements, two sets of simulations are presented – the first one with the cavity resonance along the AC direction at 1440 nm and the second one at 1495 nm, corresponding to conditions in Device D1 and D4, respectively. The

difference in spectral trajectories arise from the competition between the excitonic absorption along the AC direction and the cavity resonance and represents a tuning knob to access different polarization states.

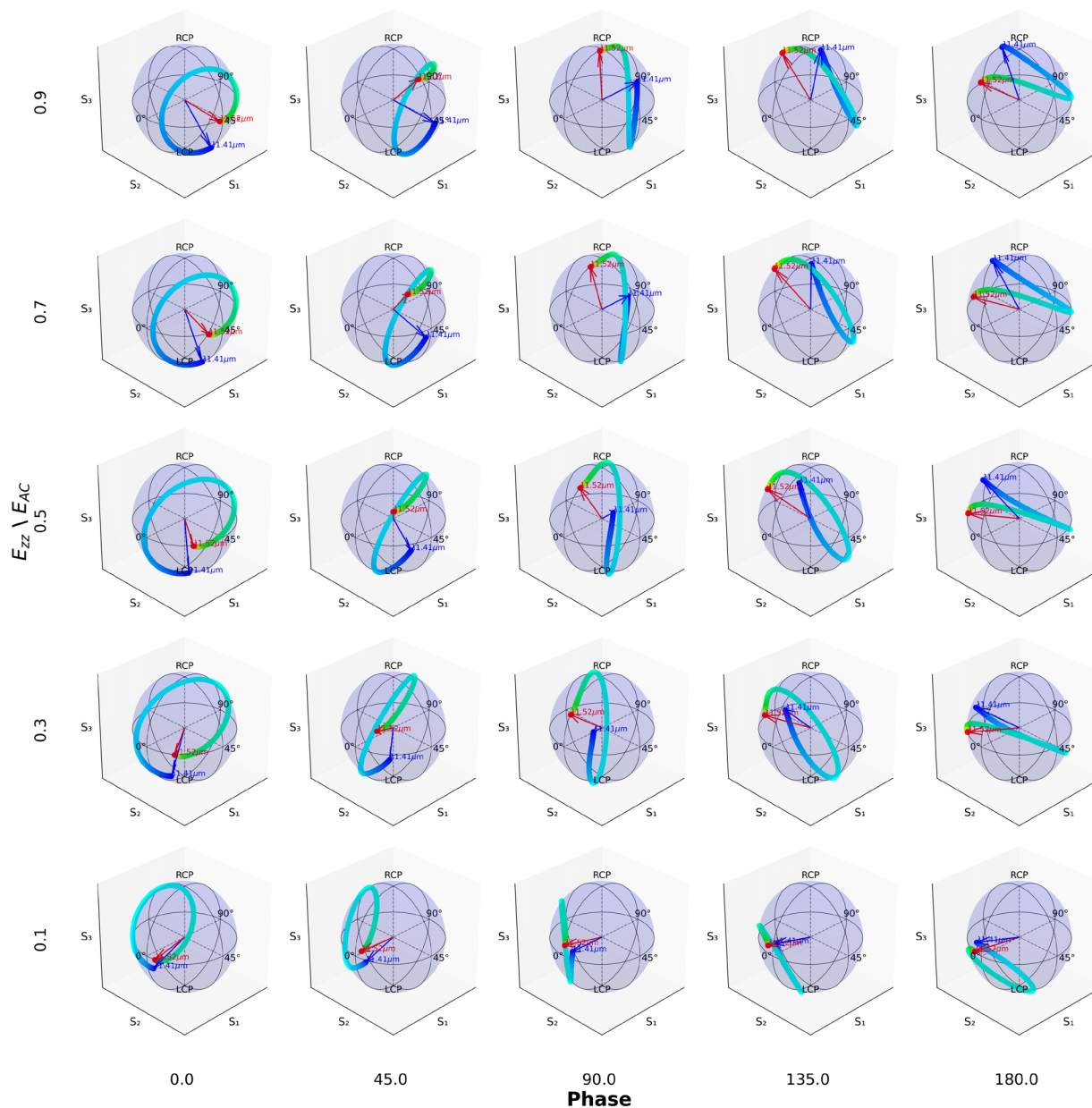


Figure S19. Polarization conversion dependence on incident polarization. Effect of the input polarization condition on the evolution of spectral trajectories on the normalized Poincaré sphere is shown. As the phase delay and the relative amplitudes are tuned between the AC and ZZ component of the incident light, different trajectories are undertaken. The cavity resonance along the AC direction is at 1440 nm. The blue (red) arrow denotes the polarization state at 1410 (1520) nm.

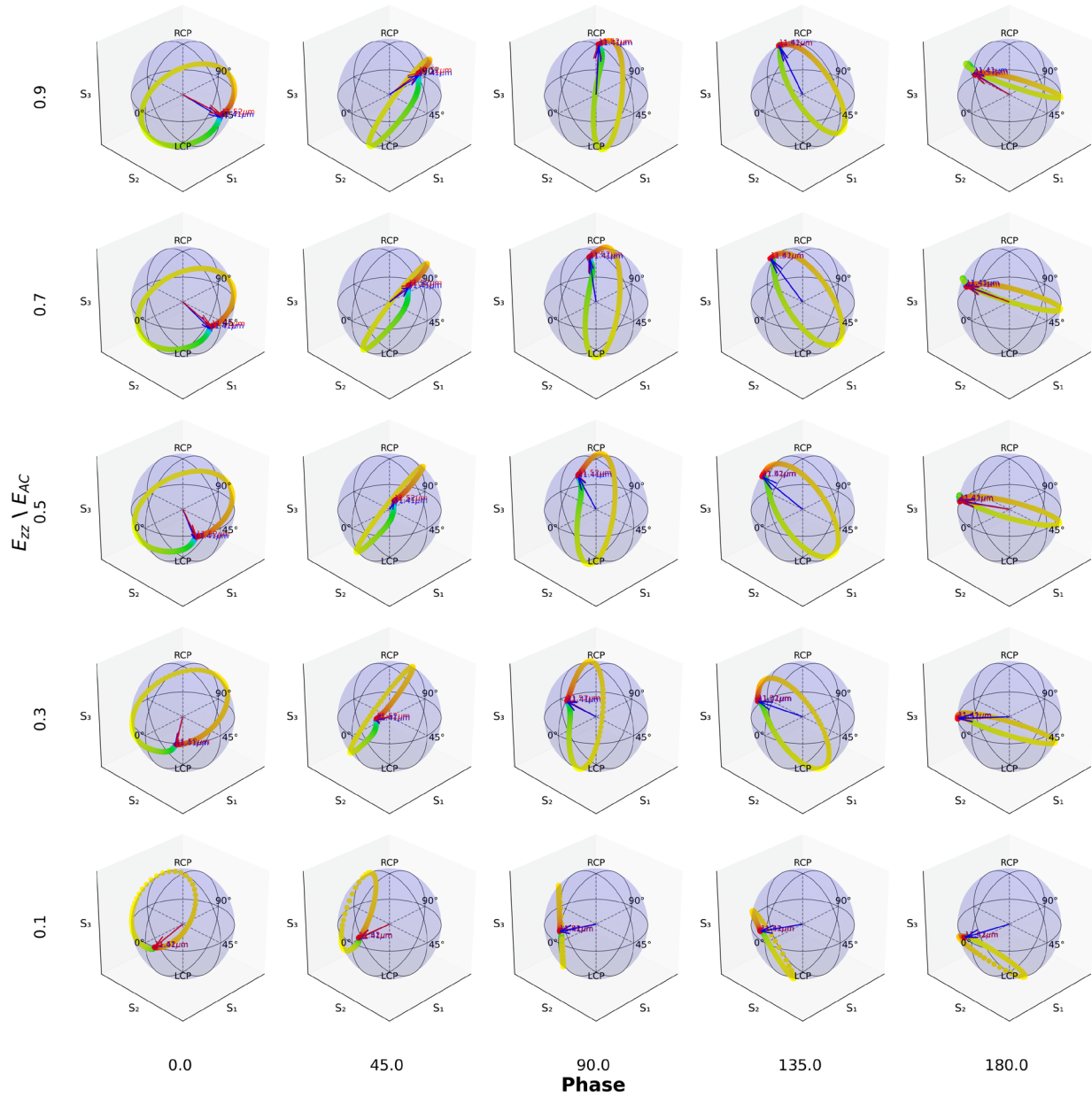


Figure S20. Polarization conversion dependence on incident polarization. Effect of the input polarization condition on the evolution of spectral trajectories on the normalized Poincaré sphere is shown. As the phase delay and the relative amplitudes are tuned between the AC and ZZ component of the incident light, different trajectories are undertaken. The cavity resonance along the AC direction is at 1495 nm. The blue (red) arrow denotes the polarization state at 1410 (1520) nm, overlapping.

S20. Numerical modelling of cavity-enabled polarization conversion

We discuss here, through numerical modelling, the effect of the different exciton parameters on the polarization conversion performance of a typical cavity. Fig S22 summarizes our findings by showing the azimuthal and ellipticity dependence on the exciton broadening, oscillator strength and the exciton resonance wavelength. The most striking impact on the polarization conversion is seen from the oscillator strength, which dictates how strong the exciton, hence the anisotropy, is. Impact of the broadening or the

resonance frequency is relatively weak on the azimuthal angle. Similarly, for ellipticity also, a strong dependence is seen on the oscillator strength. Quite interestingly, while the overall magnitude of the ellipticity resonance is reduced with decreased oscillator strength, for wavelengths slightly below 1440 nm, a non-monotonic dependence is seen. This wavelength range can be used to tune ellipticity from a low value to a high value and back to low again, making it attractive for tunable quarter-wave plate like operation. This non-monotonicity stems from the co-variation of amplitude and phase as a function of exciton parameters, which are both captured in ellipticity. With increasing doping, while the refractive anisotropy is reduced which causes the overall ellipticity change to decrease, the losses are quenched too, which increases the Q-factor of the cavity resulting in the lineshape modification and higher ellipticity for certain wavelength ranges. Small impact of broadening is seen on ellipticity, whereas a monotonic but sizeable effect is observed with resonance frequency of the exciton on the same. Cavity parameters used were - top Au = 10.5 nm, PMMA = 140 nm, top hBN = 53 nm, BP = 1.59 nm, bottom hBN = 119 nm.

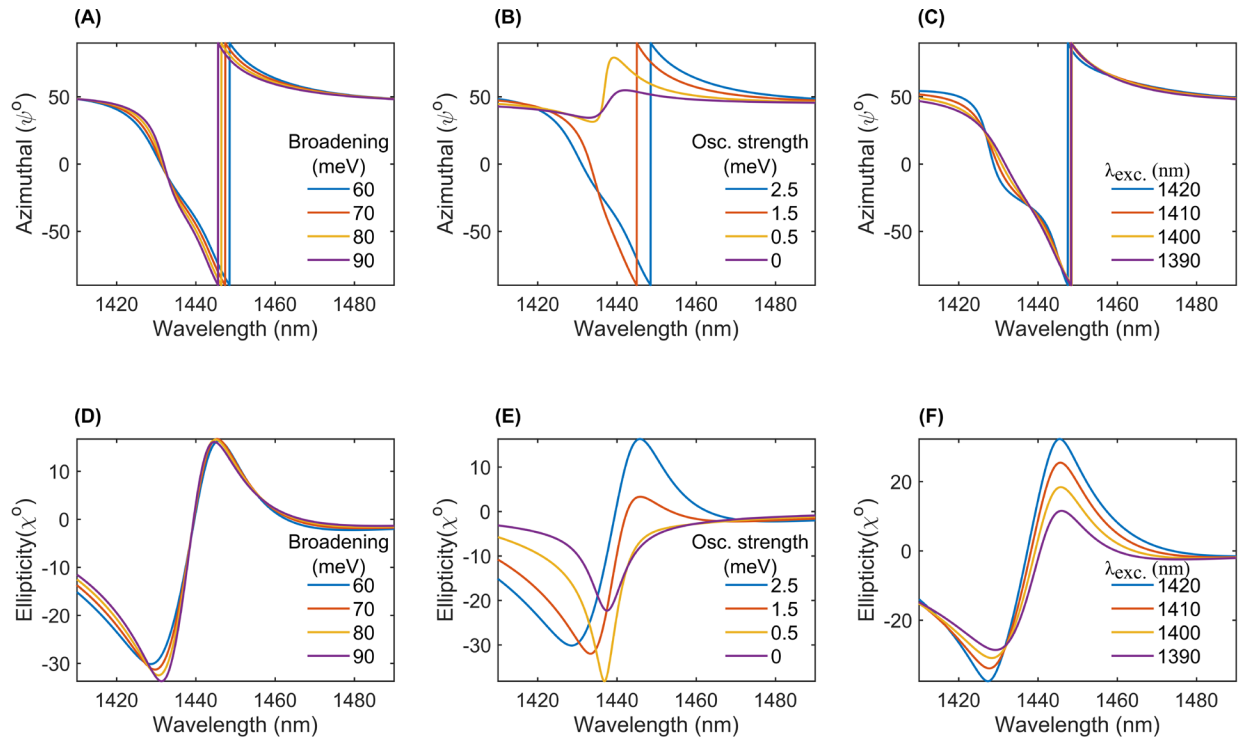


Figure S21. Polarization conversion dependence on exciton parameters in TLBP. Effect of different exciton parameters on the azimuthal and ellipticity of a typical cavity-based device. (A), (B), (C) Effect on azimuthal angle for different exciton broadening, oscillator strength and resonance wavelength, respectively. (D), (E), (F) Same as (A)-(C), but for ellipticity.

Since the polarization dynamics is most strongly tuned with the strength of the oscillator, we can numerically estimate the cavity spectral variation with doping. We plot the Stokes parameters (S_0, S_1, S_2, S_3) as a function of the oscillator strength. An excellent agreement with experimental measurements (Fig. 4 of main text) is seen, confirming that screening of the exciton due to free carriers is the major driving mechanism for polarization conversion.

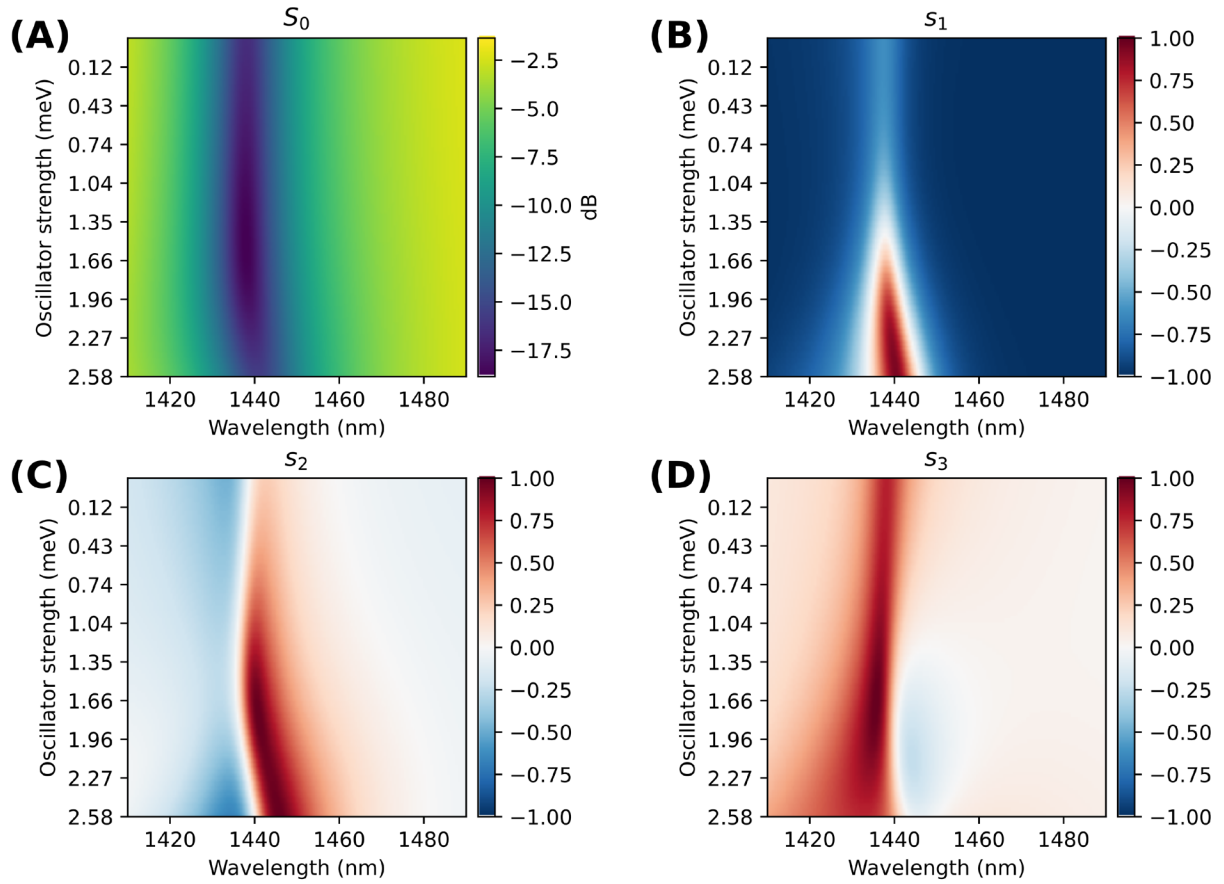


Figure S22. Numerical modelling of cavity enabled polarization conversion using the methods described in sections S12 and S13. (A) Intensity (S_0) variation with oscillator strength of the exciton in TLBP. The cavity parameters correspond to device D1. (B), (C), (D) s_1 , s_2 , s_3 showing the same. This agrees with our observation of the electrically tunable polarization conversion results in Fig. 4.

S21. Normalized Poincaré sphere dynamics and polarization ellipses for electron doping

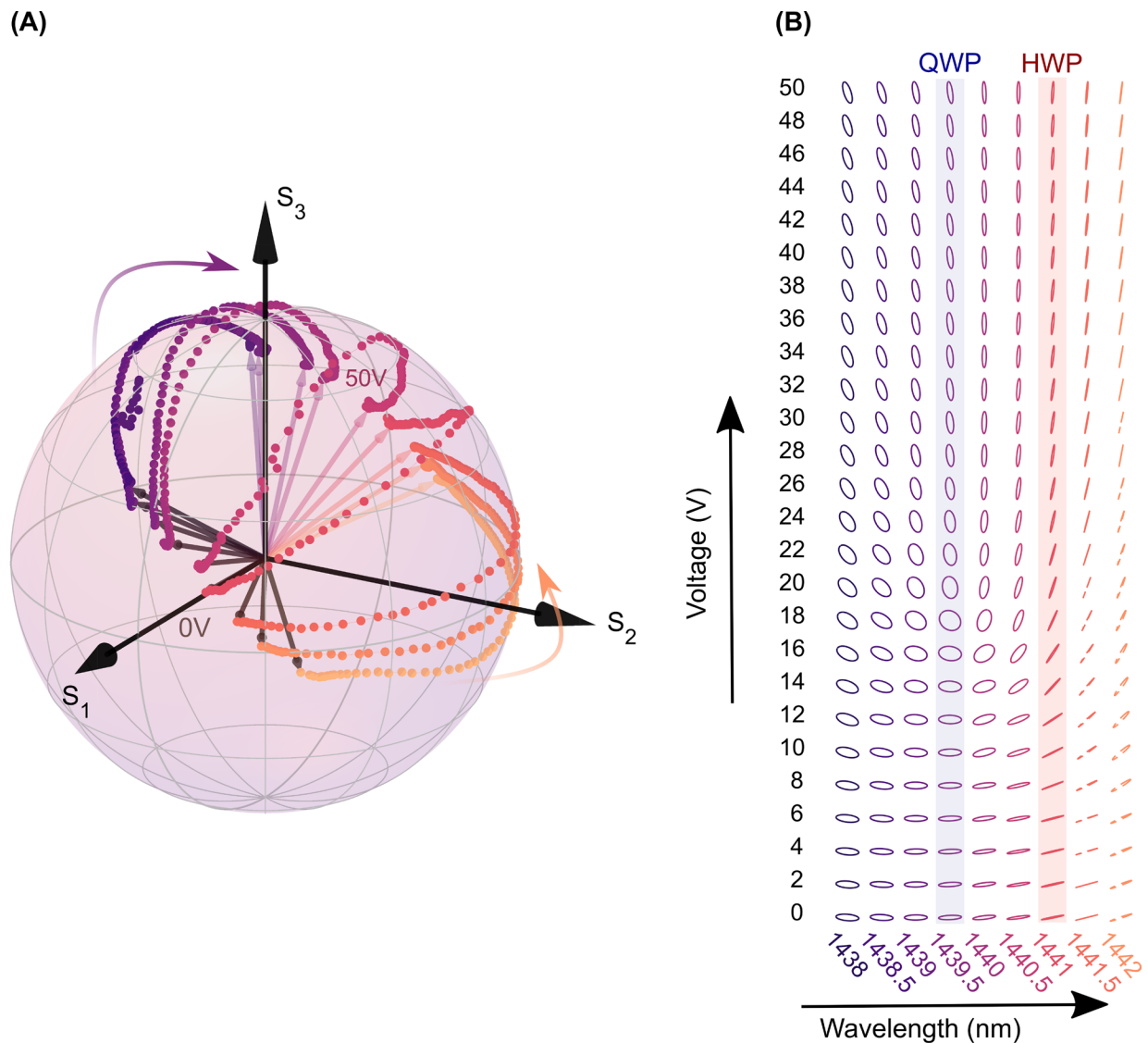


Figure S23. Normalized Poincaré sphere dynamics and polarization conversion for electron doping. (A) Voltage dependent trajectories for 9 different wavelengths from 0V to +50V (electron doping) showing highly versatile polarization generation. Colors correspond to the same 9 wavelengths shown in (B). (B) Two-dimensional map of generated polarization states as a function of wavelength and voltage for 9 wavelengths and select few voltages. Half-wave plate (HWP) like operation is seen for 1441 nm, whereas quarter-wave plate (QWP) like operation is seen for 1439.5 nm.

S22. Additional gating results from other spots on D1

Here, we discuss the gating results from other spatial positions on device D1. The general trend of the spectral trajectory collapsing in arc length is observed for all points. However, the exact trajectories traced out on the normalized Poincaré sphere are determined by the local complex refractive index of the TLBP and its gate tunability.

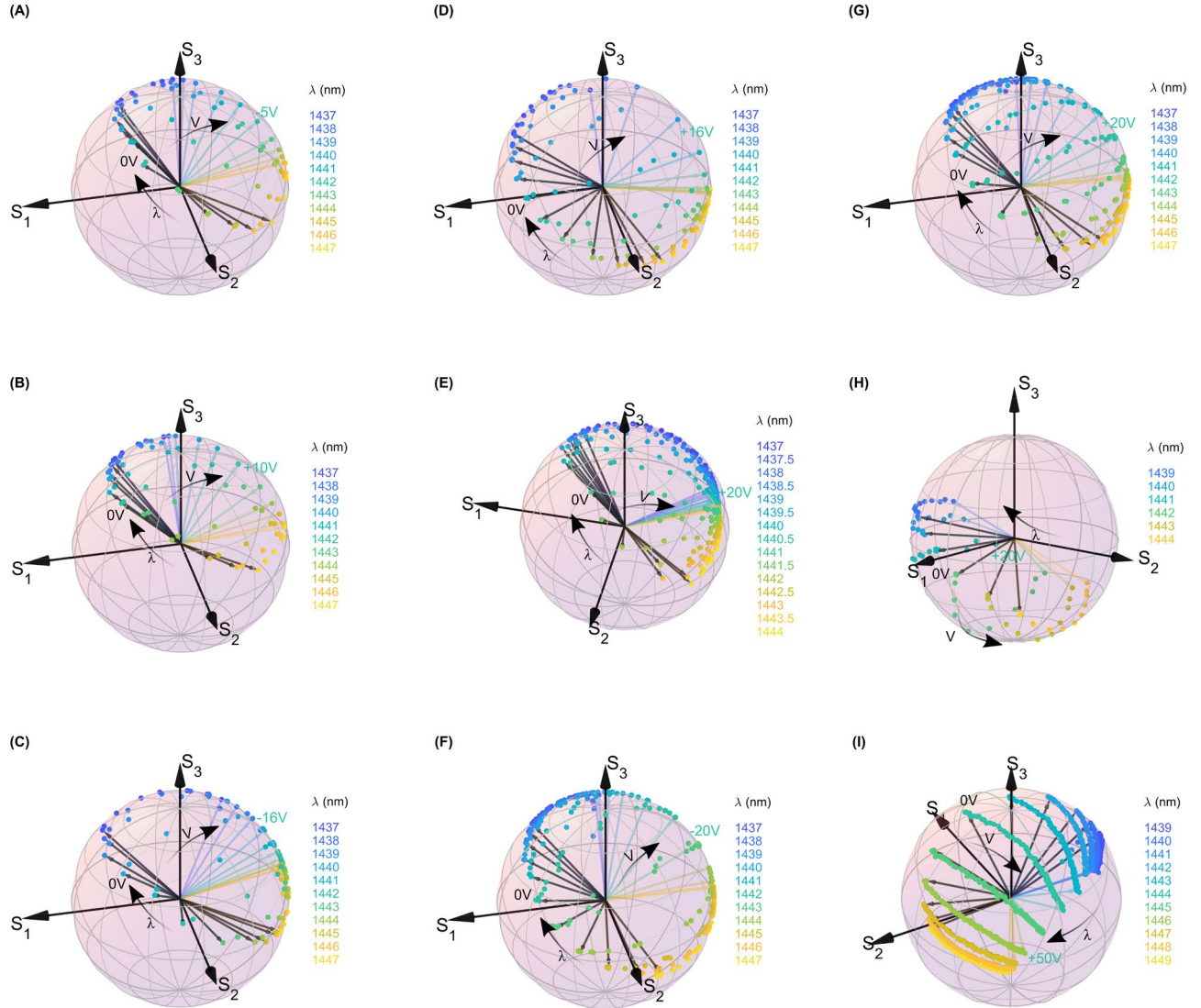


Figure S24. Normalized Poincaré sphere dynamics from additional spatial points in device D1. (A)-(I) Normalized Poincaré sphere trajectories for different wavelengths for different voltages for different spots in device D1. Each color corresponds to a different wavelength. For each color, the voltage trajectory direction is marked. Beginning and end voltage values are marked for each measurement. The dark arrows point the 0V condition for each wavelength and the light (color coded for each wavelength) arrows denote the highest voltage point.

S23. Full spectral dynamics on the normalized Poincaré sphere

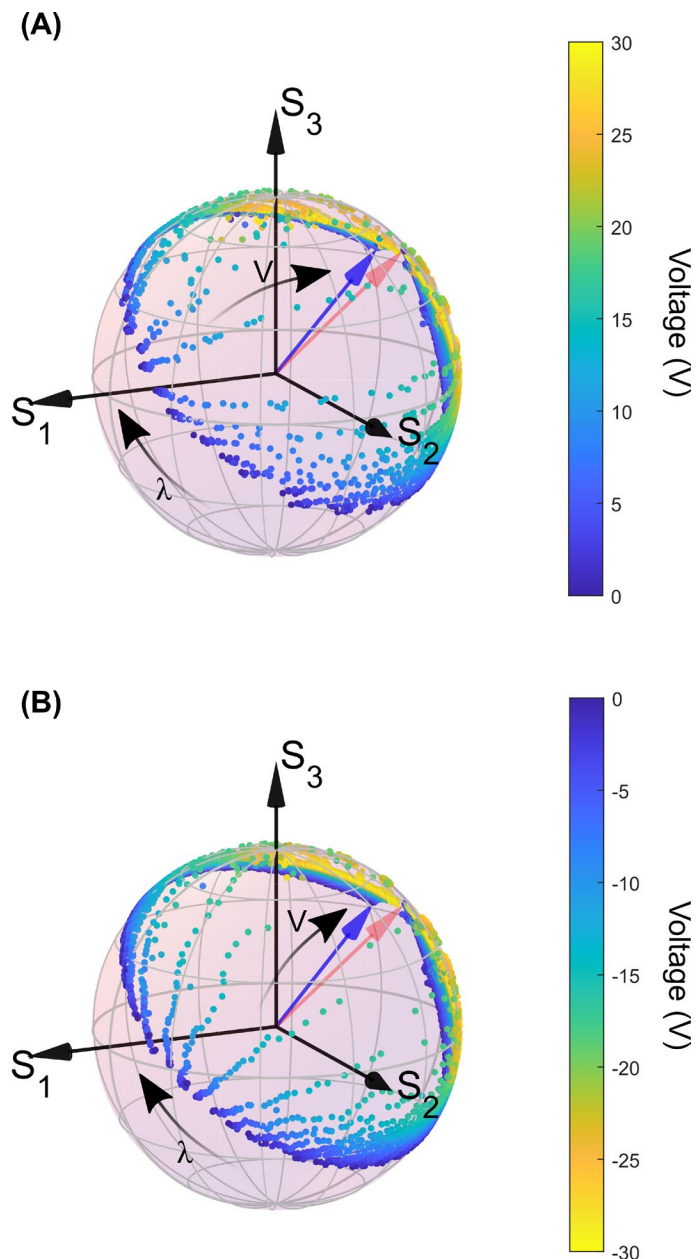


Figure S25. Spectral and voltage tuning of normalized Poincaré sphere trajectories for Device D1. (A) Evolution of polarization conversion for positive voltages (electron doping) and (B) negative voltages (hole doping). The same color represents a spectral scan (from 1410 nm to 1520 nm in steps of 0.5nm), while a color variation shows changes of the spectral trajectory with voltage from 0 to 30V for (A) and 0 to -30V for (B), in steps of 0.5V. Blue arrows represent polarization state at 1410 nm for 0V while red arrows represent the same at 1520 nm.

S24. Normalized Stokes parameter tuning on electron and hole doping

A competition between the excitonic absorption and the cavity resonance governs the overall optical response of the system, due to the close proximity of the two features. Hence, maximising the polarization conversion requires carefully adjusting the incident polarization to balance the losses along the two principle axes of TLBP for a fixed orientation of the device. To quantify the degree of polarization conversion, traces on the normalized Poincaré sphere were measured for different input ellipticity and azimuth. The longest arc was found for nearly linearly polarized input at an angle of $\sim 27^\circ$ with the AC axes of TLBP, corresponding to a vertical polarization in the lab frame.

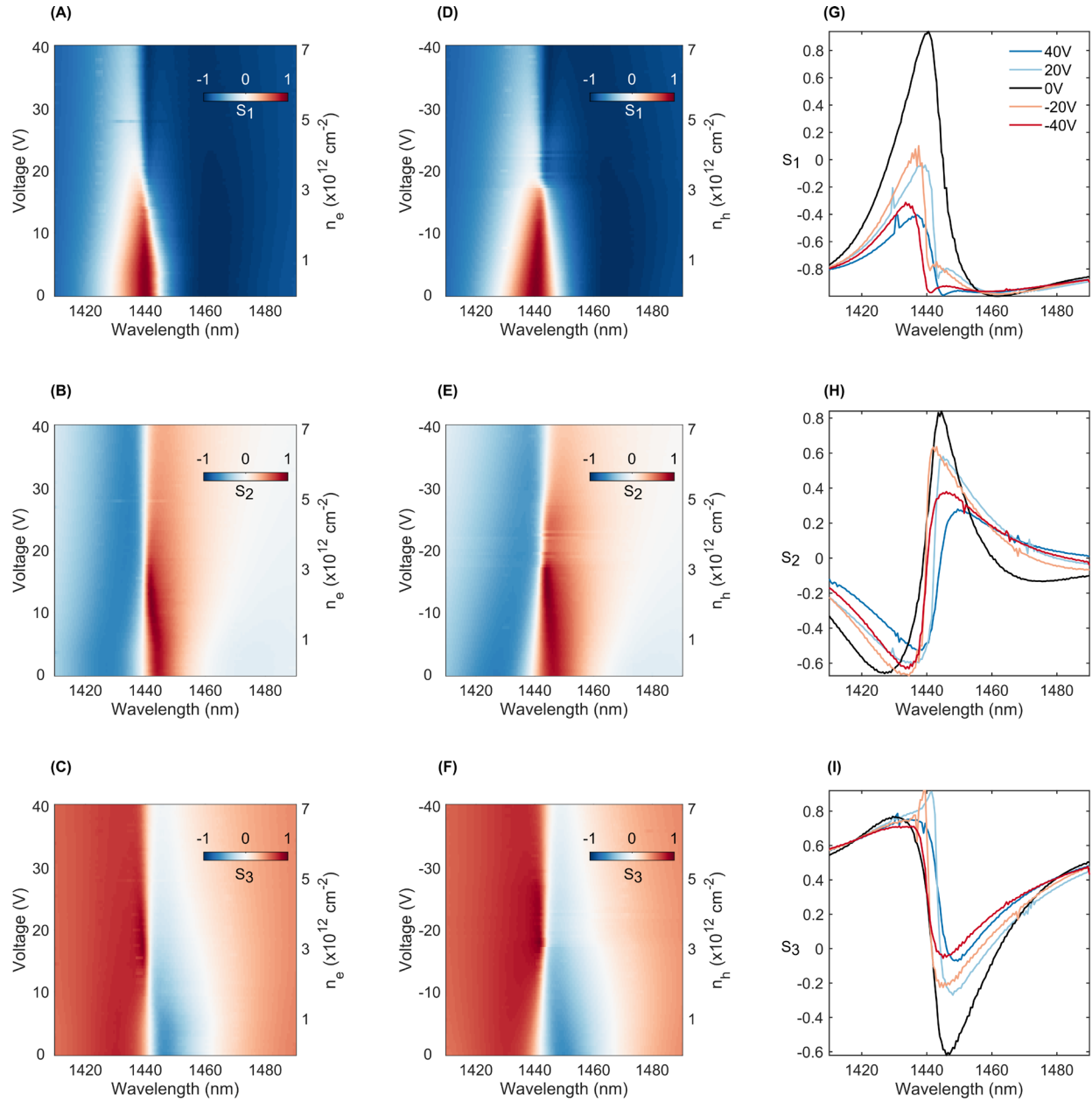


Figure S26. Normalized Stokes parameters with electron and hole doping. (A),(B),(C) False colormaps of the evolution of the three normalized Stokes parameters (s_1, s_2, s_3), determining the polarization state of the reflected light, as a function of wavelength and positive voltages (for electron doping). The results are from device D1. Continuous tuning of all the 3 parameters can be seen around the cavity resonance ($\sim 1440\text{nm}$) for the entire range of doping, illustrating efficient tuning of the polarization state with voltage. (D),(E),(F) Same as (A),(B),(C) but for negative voltages (for hole doping), showing similar changes as the electron doped side. The nearly symmetric nature of the doping dependence shows that at 0V, the device is at charge neutral conditions. (G),(H),(I) Line cuts taken from the false colormaps for the three normalized Stokes parameters (s_1, s_2, s_3 respectively) for 5 different voltages (0V, 20V, 40V, -20V, -40V) to visualize the changes with higher clarity.

S25. Reflectance change on electron and hole doping

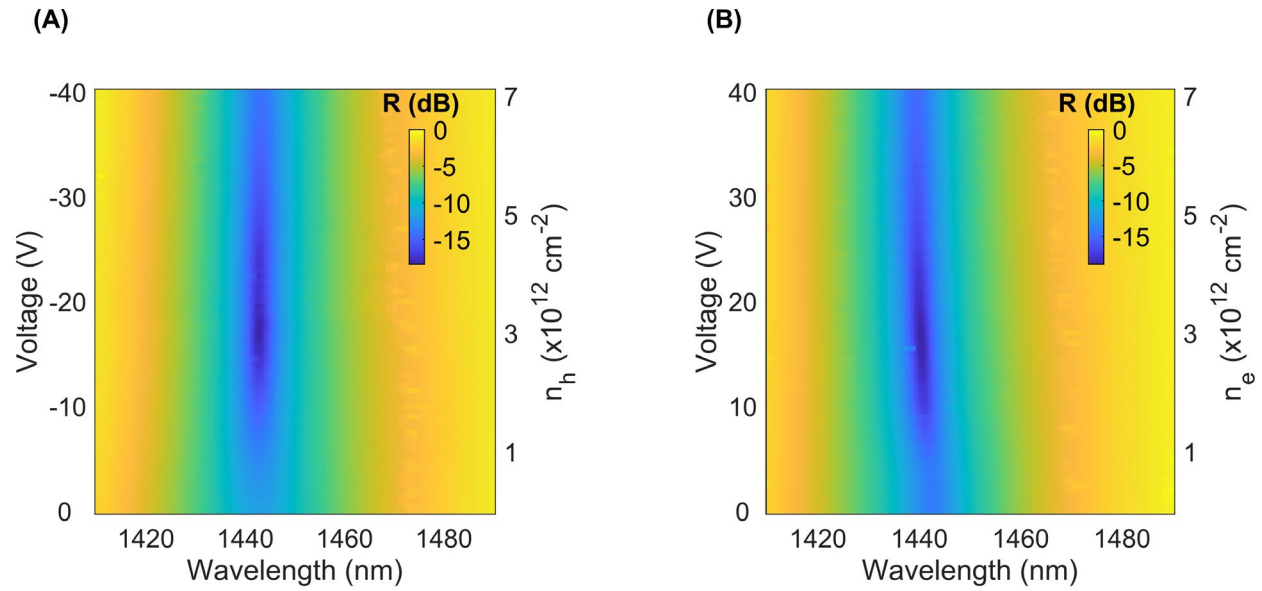


Figure S27. Reflectance change (S_0) of the cavity upon electron and hole doping. (A), (B) show the change in the reflectance (Stokes intensity S_0) of the device D1 as a function of wavelength for different applied voltages on the hole doping and electron doping side, respectively. The colormaps are plotted in dB for better clarity.

S26. Azimuthal and ellipticity changes on electron and hole doping

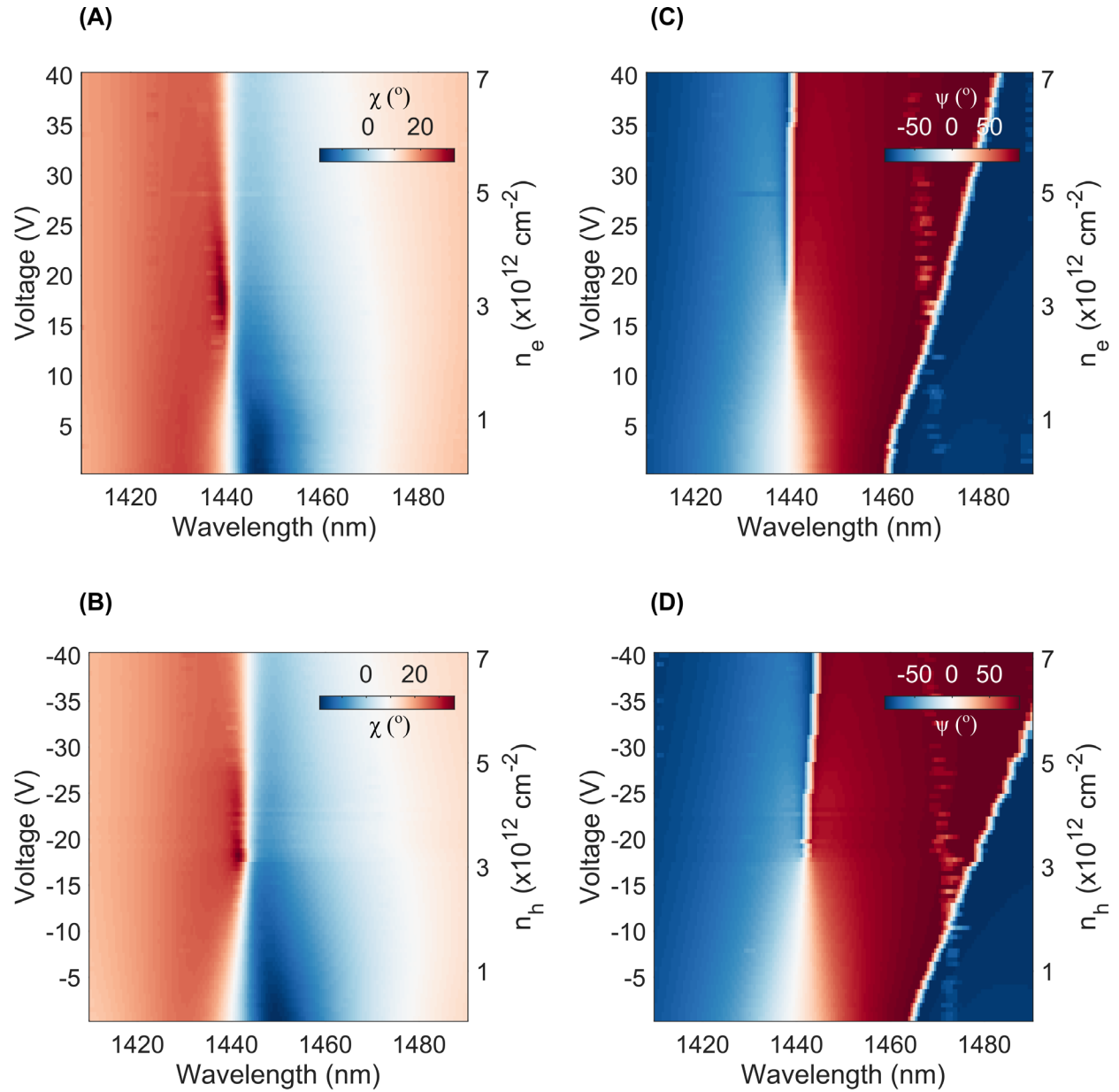


Figure S28. Azimuthal and ellipticity angle change upon electron and hole doping. (A), (B) show the changes in the ellipticity angle (χ), in degrees, of the device D1 as a function of wavelength for different applied voltages on the electron doping and hole doping side, respectively. (C), (D) show the same as (A) and (B), but for the azimuthal angle (ψ), in degrees. The abrupt jump in the azimuthal angle is a numerical artifact arising from the indistinguishability between $+90^\circ$ and -90° .

S27. Additional gating results from a 5-layer BP device

We present here electrically tunable reflection contrast measurements performed on a 5-layer BP sample. The device geometry is the same as the one adopted for 3-layer devices (hBN-BP/FLG-hBN/Au). Fig. S29A shows the reflection contrast along armchair (AC) and zigzag (ZZ) directions. A strong excitonic feature at $2\ \mu\text{m}$ is seen along the AC direction, while a featureless spectrum is seen along the ZZ direction. Upon application of gate voltage, strong modulation of the reflectivity is seen. Fig. S29B summarizes the results demonstrating the same. The changes are visualized better when normalized to the reflectivity at 0 V. The strongest modulation is seen at $2\ \mu\text{m}$, which confirms that the origin of this electro-optic response originates from the exciton dynamics. These measurements were performed using a Fourier transform infrared (FTIR) white light source coupled with an infrared microscope in ambient conditions. These measurements demonstrate that efficient polarization conversion can also be achieved at much longer wavelengths ($\sim 2\ \mu\text{m}$) due to the large excitonic tunability. In fact, the thickness of BP can be tuned, and the operation wavelength can span the entire visible (750 nm) to mid and far-IR range ($\sim 3\text{-}20\ \mu\text{m}$).

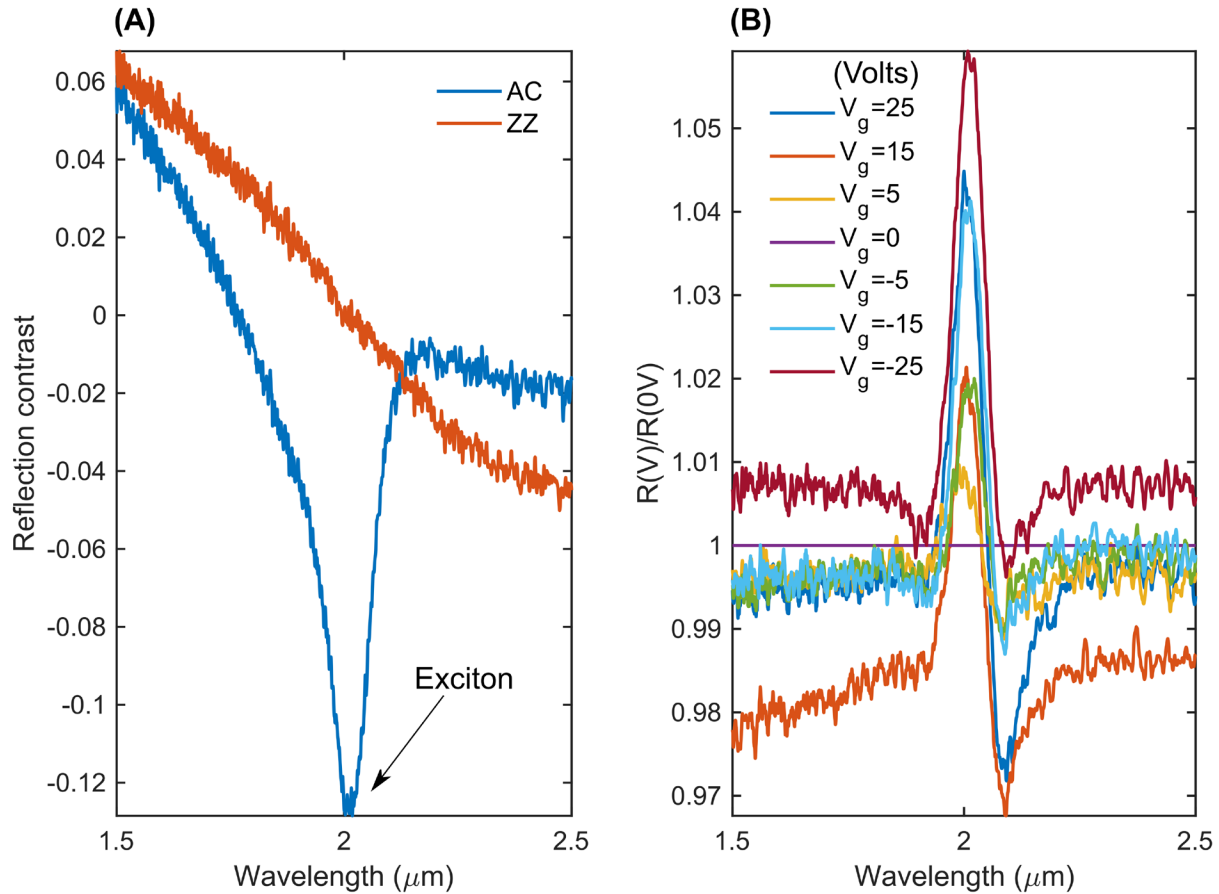


Figure S29. Gate-dependent reflectivity modulation in 5-layer BP device. (A) Reflection contrast showing excitonic feature along the AC direction and a featureless spectrum along the ZZ direction. (B) Relative reflection (w.r.t. 0V) shows strong modulation under different applied biases, with the strongest tuning near the excitonic resonance.

S28. Choice of three-layer BP (TLBP)

We motivate here why TLBP was used in the study over other thicknesses of BP. The choice of three-layers is primarily driven by the compelling technological advantages of constructing electro-optic modulators in the telecom band such as for optical fiber communication (typical losses are ~ 0.2 dB/km at $1.5 \mu\text{m}$ as compared to 8 dB/km at 640 nm), quantum networks and photonic integrated circuits (based on Silicon). Previous reports on layer-dependent bandgap in BP support the fact that BP is well suited for operation from visible to mid-IR. Furthermore, these studies clearly show the evolution of the optical bandgap (excitonic resonance) in BP as a function of layer thickness. While the optical bandgap is in the visible (~ 750 nm) for monolayer BP, it saturates at $\sim 4 \mu\text{m}$ for $>20\text{nm}$ thin films. Three layers hits the sweet spot with an excitonic resonance ~ 1400 nm, particularly suited for the window of telecom operation.

Furthermore, the electrical tunability of such optical transitions is expected from similar studies in monolayer TMDCs and few-layer BP. The key physics driving the polarization conversion tunability (or in general terms, tuning the exciton polarizability) is the suppression of excitons due to screening by induced free charges (S8, S9). These effects are most prominent for monolayer TMDCs owing to their direct bandgap and strong excitons, while for bilayer or multilayer TMDCs, the bandgap becomes indirect, and the magnitude of electrically driven changes reduce. However, for BP, because of the band minima being at the Γ -point (arising out of D_{2h}^{18} point group crystal symmetry), the direct nature of the bandgap is always maintained and thus the excitonic effects and its tunability remain quite significant at the few-layer limit, as shown in our work, for both TLBP and 5-layers BP (S27). The modulation fraction decreases as the thickness of BP is increased, which stems from the finite Thomas-Fermi screening length that governs the amount of effective modulation depth in the vertical direction in a semiconductor channel. Such length scales are typically of order $\sim 2\text{-}3$ nm for the charge densities accessed here for BP; anything thicker is effectively not modulated beyond the Thomas-Fermi screening length. The Thomas-Fermi screening length can be visualized in the following plot:

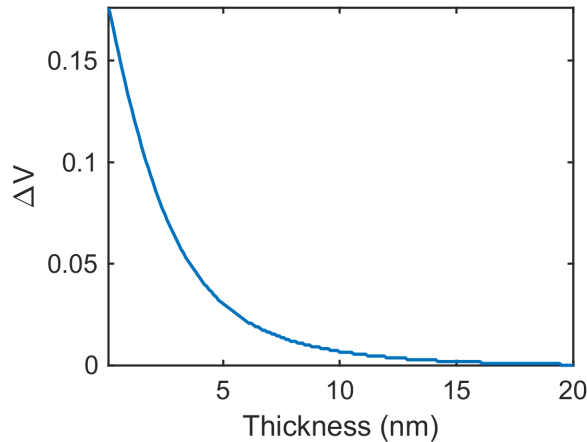


Figure S30: Thomas-Fermi screening effect in BP. Band-bending in multilayer BP as a function of thickness for a charge density of $5 \times 10^{12}/\text{cm}^2$. A Thomas-Fermi screening length (λ_{TF}) of 2.9 nm is obtained.

To summarize, both the bandgap being conveniently in the telecom band along with the high electrical tunability of the exciton drives our choice of three-layers BP (TLBP). The same effect can however be shown in monolayer BP in the visible/NIR (600-900 nm), bilayer BP in the NIR (900-1200 nm), and so on and so forth. Finally, the degree of polarization conversion will ultimately depend on the coupling between the cavity and free space and hence the cavity would need to be designed for the right working wavelength.

S29. Comparison of polarization conversion mechanism with liquid crystals

The distinction between bulk materials and excitonic 2D semiconductors, particularly TLBP in this case, is quite important. While the electro-optic operation hinges on the physical re-orientation of the dipoles for bulky materials like liquid crystals, such is not the case for 2D excitons. The physical mechanism of the operation of our device is the screening effect of the excitons by the excess induced charges in TLBP which eventually effect the dipole oscillator strength (S8, S9). The vertical electric field that is generated in the capacitor (hBN in our devices) alters the charge density in the TLBP – which acts as the other plate of the parallel plate capacitor (the back Au is the first plate). This causes the quasi-1-D dipoles which are in-plane to be affected by the out of plane electric field from the capacitor. Thus, when a normally incident light interacts with the heterostructure, the in-plane dipoles influence the in-plane electromagnetic fields. Previous measurements of tuning the dipole strength in TMDCs have also leveraged this strong vertical-field induced doping to tune the interaction with an in-plane optical field. However, due to lack of crystal symmetry breaking in the in-plane direction, such efforts have failed to control polarization.

It is also important to note, that thus far, no evidence points to actual reorientation of the dipoles (initially along x-direction) with gating, but rather a reduction in the oscillator strength and enhanced scattering.

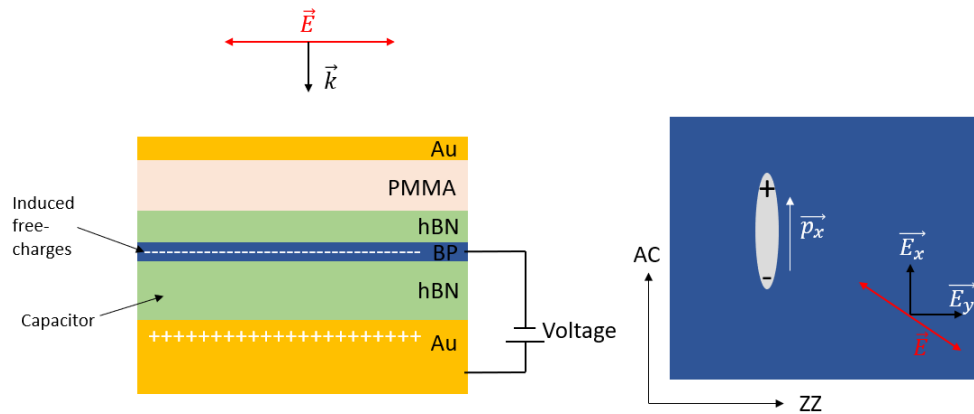


Figure S31: Dipole interaction with optical field in TLBP. Side view of capacitor geometry of working BP device. The two plates of the parallel-plate capacitor are the BP and the back Au electrode/reflector. Free carriers are induced in the BP with applied voltage. Incident optical field (polarized in the in-plane direction, perpendicular to the vertical capacitor field) is shown, along with the Poynting vector. A top view of the BP flake along with the dipole orientation is shown, with the Armchair (AC) and Zigzag (ZZ) axes marked. Incident field (in-plane) can be decomposed along the AC and ZZ direction, marked as x and y respectively. The x-component is strongly influenced by the exciton-enhanced cavity interaction (which is also electrically tuned), whereas the y-component is only influenced by the cavity and not the exciton and thus is not tuned.

S30. Cyclic measurements for electrically tunable devices

Multiple cyclic measurements were done on all gate tunable devices, and the results are highly consistent. No noticeable hysteresis was observed when the voltages were swept in a cyclic fashion. The cyclic scheme adopted in this work is as follows: 0V to +20V, back to 0V, to -20V and then back to 0V (for Fig. S33). The normalized Stokes parameters (s_1, s_2, s_3) and the voltage sequence for one such device (D1) is shown in Fig. S32.

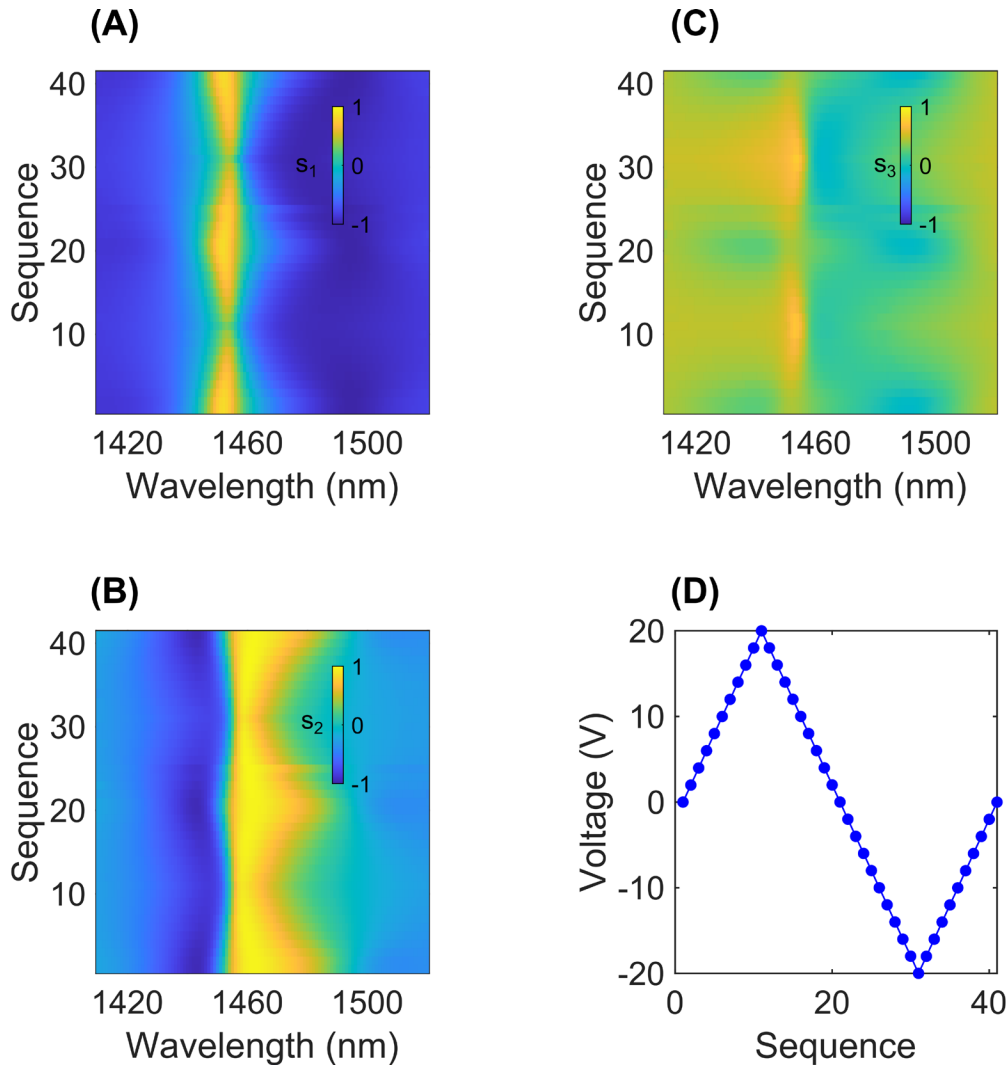


Figure S32. Cyclic Stokes measurements. (A), (B), (C) Normalized Stokes parameters (s_1 , s_2 , s_3) spectra measured as a function of voltage in a cyclic fashion. (D) The applied voltage as a function of the sequence number.

S31. Discussion about edge effects in spatial mapping of polarization conversion

“Edge effects” may result from the convolution of an atomically sharp edge encountered at the end of a BP flake and a gaussian beam, in the spatial maps presented in the main text (Fig. 3) and in Supplementary Information (Fig. S16, S17). In the current measurement configuration, we are limited by the optical diffraction limit, and it is not possible to resolve an atomically sharp edge. Thus, a true edge is not measured, rather it is convolved with the nearest pixel. So, near the edges, the ellipticity appears reduced because the finite size ($\sim 1.5\text{-}2\ \mu\text{m}$) gaussian beam samples both the BP flake + cavity and the no-BP cavity only region. Furthermore, the blueshift in the resonance compared to the interior of the BP flake can be understood from the fact that the beam is sampling less material or reduced cavity length (as it scans half a TLBP and half a missing BP region – for example) and thus the cavity resonance blueshifts. To prevent a convolution of the edge effect and true polarization dynamics, all the gate tunable and passive device measurements shown in the paper have been done in the interior of the samples and not at the edges. Further higher resolution measurements, such as tip-based near field microscopy, would be required to address if there are any true

edge effects, such as edge lattice reconstruction and how that influences the polarization conversion. An illustration of the finite size of the beam and the sampling effect is shown for further clarity in Fig. S33.

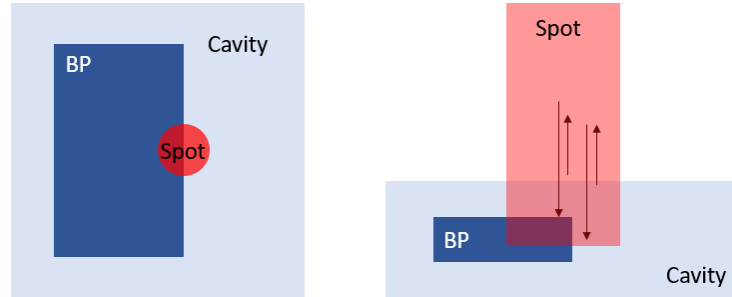


Figure S33. Edge effects in spatial mapping. Top view and side view illustration of cavity and BP, along with the gaussian (diffraction limited) beam at the edge showing sampling from both the regions leading to different polarization conversion at the edge compared to the interior of the sample (spot size is exaggerated for clarity).

S32. Outlook towards high efficiency polarization modulators based on BP

Our current work illustrates the versatility of using BP, especially TLBP (for telecom band), as an active material for polarization conversion. In the current scheme of operation in a modest quality factor cavity and sufficiently close to the excitonic feature, the overall reflectivity of the devices is low. Several ways may be adopted to boost this efficiency to a higher value. Firstly, to increase the overall reflectivity, high-Q cavities (such as photonic crystal cavities, DBR-based Fabry-Pérot cavities, etc.) can be combined with BP at sufficiently detuned wavelengths (detuned from excitonic resonance) to reduce the losses in the system. This obviously requires a judicious choice of thickness for BP depending upon the working wavelength. For example, at 1550 nm, we expect bilayer (or even monolayer) BP to be a good candidate. Furthermore, to increase the doping concentration and thus the modulation depth, higher dielectric permittivity materials such as HfO₂ can be used. This has been shown to be an effective strategy for low-loss electro-optic modulation (21) recently for TMDCs. Better growth of higher quality BP crystals showing prominent excitonic behavior on different substrates is needed however to make this a viable strategy. Here, we show numerically how such a design would work using experimentally measured complex refractive indices for TLBP and integrated with an ultra-low loss dielectric mirror based Fabry-Pérot cavity, operating at a sufficiently detuned wavelength. The structure considered here consists of a top DBR of 20 pairs of SiO₂/SiN_x (n=1.45/1.87), TLBP, 10-nm gate dielectric Al₂O₃ (n=1.73), a buffer layer of SiN_x (n=1.87) to adjust the cavity resonance, a bottom DBR of 40 pairs of AlAs/Al_{0.1}Ga_{0.9}As (n=3.5/3.05) and a GaAs substrate (n=3.55). The refractive indices for AC BP and AC-doped BP were taken from measurements done at 0V and 50V (hole doping) as noted in Fig. 1(C) and 1(D) of the main text. As can be seen for a working wavelength of 2986.6 nm a phase shift of $\sim 2\pi$ can be obtained between undoped and doped conditions, whereas the reflectance stays extremely high (>95%) for the same wavelength. Similarly, the top and bottom pairs can be appropriately designed to maintain high reflection all throughout the spectral window, with a slight compromise in the achieved phase shift. Here, we show the performance of the same design with 17 top pairs (instead of 20), which gives us a maximal phase shift of $\sim 1.55\pi$ with over 90% reflection at the working wavelength, but also maintaining >65% for the entire spectral range which is already an extremely high reflection efficiency.

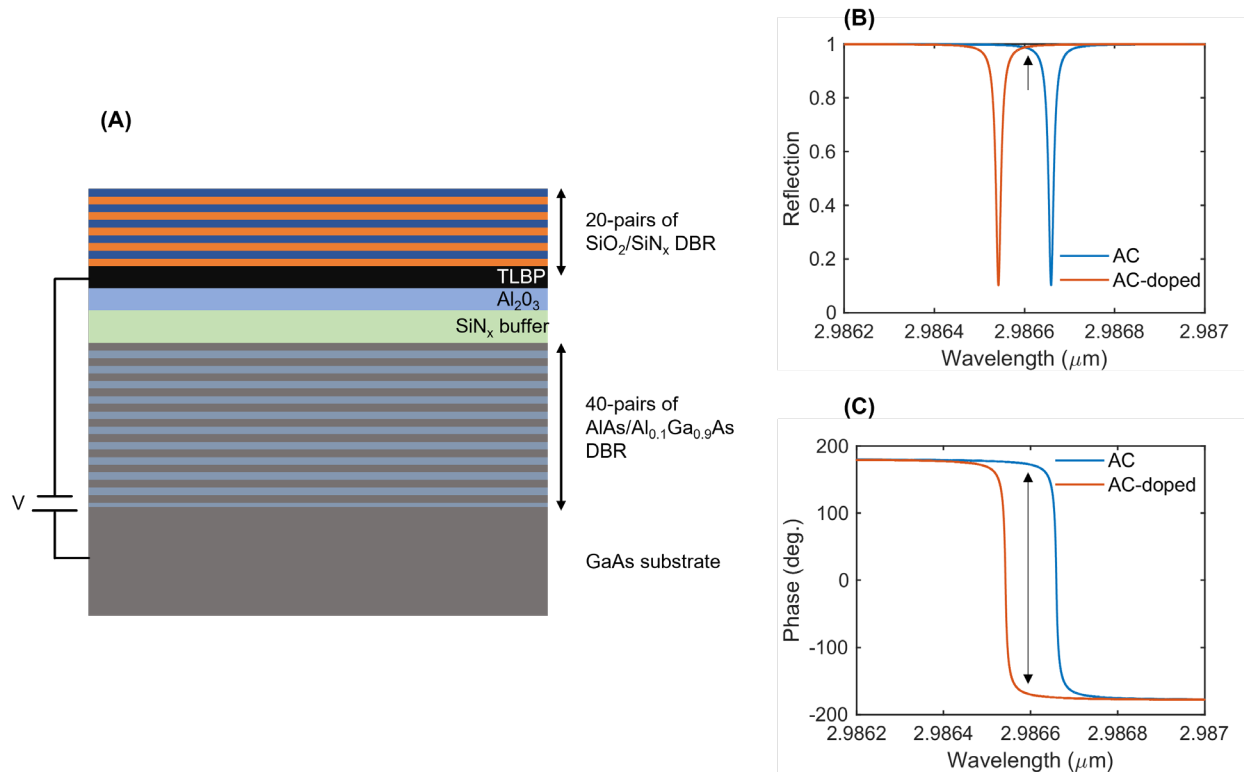


Figure S34. High efficiency numerical design for polarization conversion. (A) Double DBR based Fabry-Perot cavity design incorporating BP. (B) Reflection and (C) phase from the corresponding cavity structure for pristine and doped armchair (AC) direction.

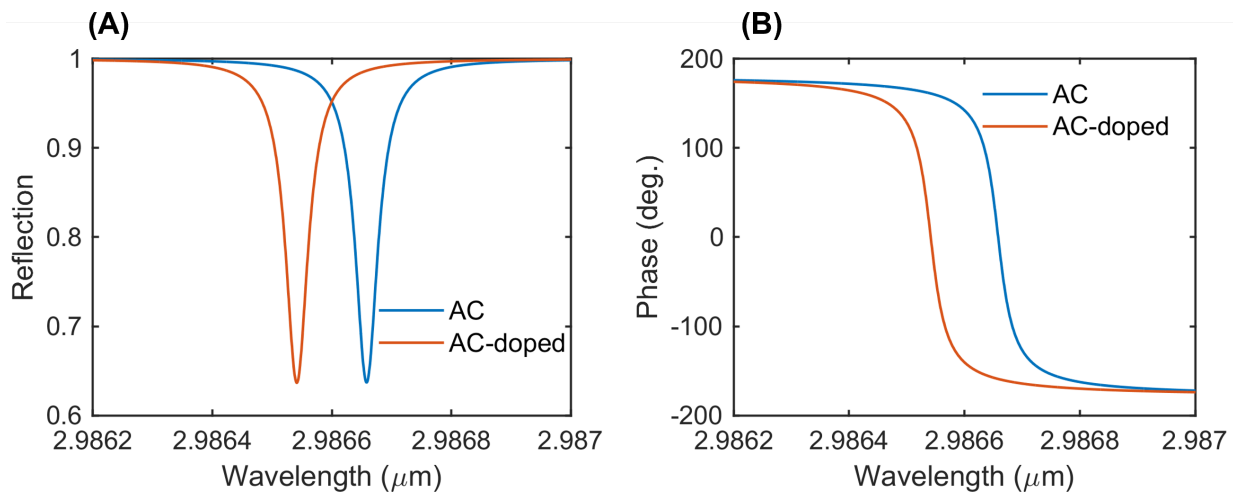


Figure S35. High efficiency numerical design for polarization conversion. (A) Reflection and (B) phase from the proposed cavity structure in Fig. S34 for pristine and doped armchair (AC) direction for 17-top pairs instead of 20.

Furthermore, for two-state polarization switching devices (applications requiring switching between two-states of polarization such as linear to circular polarization), the design can be tuned to have no amplitude modulation and only polarization modulation. An illustration of this can be already seen in our current working devices. For example, if we analyze the intensity, ellipticity and azimuthal for hole doping in

Fig. S36, around 1450 nm, minimal change in intensity (<0.3 dB) and azimuthal angle is seen with significantly large change in ellipticity ($\sim 21^\circ$) between 0V, -20V and -40V. Such designs may be further optimized by tuning the cavity resonance for wavelength of interest.

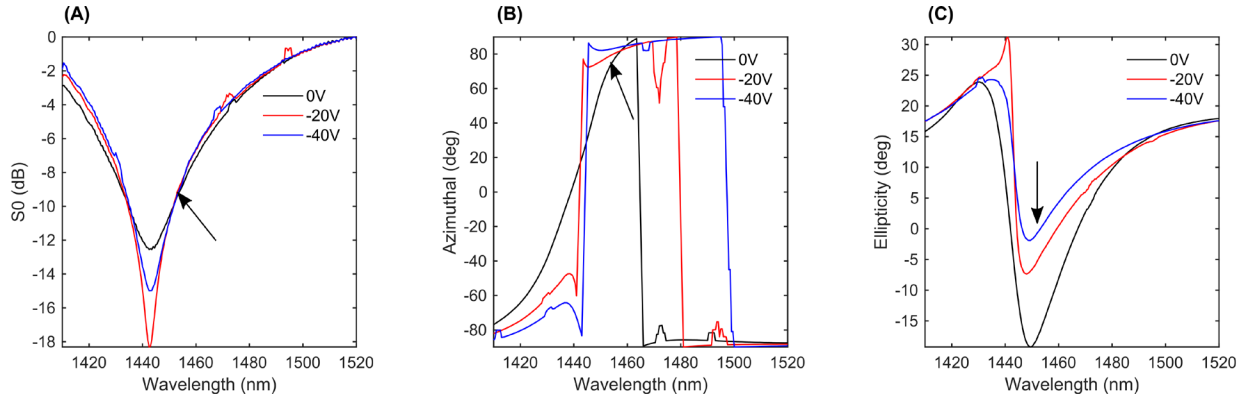


Figure S36. Amplitude, azimuthal and ellipticity line cuts for hole doping. (A) Amplitude spectrum for three distinct voltages (0V, -20V, -40V) corresponding to hole doping, showing variation in the intensity at the resonance. (B), (C) Same as (A) but for azimuthal and ellipticity angle. A region around 1450 nm can be identified to have nearly constant amplitude modulation, minimal azimuthal change but large ellipticity modulation.

Finally, we comment on the possibility of complete independent control of both amplitude and phase which requires multiple degrees of freedom (at least 2). We believe judicious dual gate designs, multiple cascaded BP unit-cells and hetero structuring with a broadband lossy material, like graphene, to balance the losses in the two system to keep the amplitude constant, might pave the way towards such control.

References and Notes

1. S. Fleischer, Y. Zhou, R. W. Field, K. A. Nelson, Molecular orientation and alignment by intense single-cycle THz pulses. *Phys. Rev. Lett.* **107**, 163603 (2011). [doi:10.1103/PhysRevLett.107.163603](https://doi.org/10.1103/PhysRevLett.107.163603) [Medline](#)
2. G. P. Crawford, J. N. Eakin, M. D. Radcliffe, A. Callan-Jones, R. A. Pelcovits, Liquid-crystal diffraction gratings using polarization holography alignment techniques. *J. Appl. Phys.* **98**, 123102 (2005). [doi:10.1063/1.2146075](https://doi.org/10.1063/1.2146075)
3. S. G. Demos, R. R. Alfano, Optical polarization imaging. *Appl. Opt.* **36**, 150–155 (1997). [doi:10.1364/AO.36.000150](https://doi.org/10.1364/AO.36.000150) [Medline](#)
4. M. Schubert, T. E. Tiwald, C. M. Herzinger, Infrared dielectric anisotropy and phonon modes of sapphire. *Phys. Rev. B Condens. Matter Mater. Phys.* **61**, 8187–8201 (2000). [doi:10.1103/PhysRevB.61.8187](https://doi.org/10.1103/PhysRevB.61.8187)
5. X. Ling, S. Huang, E. H. Hasdeo, L. Liang, W. M. Parkin, Y. Tatsumi, A. R. T. Nugraha, A. A. Puretzky, P. M. Das, B. G. Sumpter, D. B. Geohegan, J. Kong, R. Saito, M. Drndic, V. Meunier, M. S. Dresselhaus, Anisotropic electron-photon and electron-phonon interactions in black phosphorus. *Nano Lett.* **16**, 2260–2267 (2016). [doi:10.1021/acs.nanolett.5b04540](https://doi.org/10.1021/acs.nanolett.5b04540) [Medline](#)
6. A. Crespi, R. Ramponi, R. Osellame, L. Sansoni, I. Bongioanni, F. Sciarrino, G. Vallone, P. Mataloni, Integrated photonic quantum gates for polarization qubits. *Nat. Commun.* **2**, 566 (2011). [doi:10.1038/ncomms1570](https://doi.org/10.1038/ncomms1570) [Medline](#)
7. Y. Yu, Y. Yu, L. Huang, H. Peng, L. Xiong, L. Cao, Giant gating tunability of optical refractive index in transition metal dichalcogenide monolayers. *Nano Lett.* **17**, 3613–3618 (2017). [doi:10.1021/acs.nanolett.7b00768](https://doi.org/10.1021/acs.nanolett.7b00768) [Medline](#)
8. E. Feigenbaum, K. Diest, H. A. Atwater, Unity-order index change in transparent conducting oxides at visible frequencies. *Nano Lett.* **10**, 2111–2116 (2010). [doi:10.1021/nl1006307](https://doi.org/10.1021/nl1006307) [Medline](#)
9. S. Niu, G. Joe, H. Zhao, Y. Zhou, T. Orvis, H. Huyan, J. Salman, K. Mahalingam, B. Urwin, J. Wu, Y. Liu, T. E. Tiwald, S. B. Cronin, B. M. Howe, M. Mecklenburg, R. Haiges, D. J. Singh, H. Wang, M. A. Kats, J. Ravichandran, Giant optical anisotropy in a quasi-one-dimensional crystal. *Nat. Photonics* **12**, 392–396 (2018). [doi:10.1038/s41566-018-0189-1](https://doi.org/10.1038/s41566-018-0189-1)
10. L. H. Nicholls, F. J. Rodríguez-Fortuño, M. E. Nasir, R. M. Córdova-Castro, N. Olivier, G. A. Wurtz, A. Zayats, Ultrafast synthesis and switching of light polarization in nonlinear anisotropic metamaterials. *Nat. Photonics* **11**, 628–633 (2017). [doi:10.1038/s41566-017-0002-6](https://doi.org/10.1038/s41566-017-0002-6)
11. A. H. Dorrah, N. A. Rubin, A. Zaidi, M. Tamagnone, F. Capasso, Metasurface optics for on-demand polarization transformations along the optical path. *Nat. Photonics* **15**, 287–296 (2021). [doi:10.1038/s41566-020-00750-2](https://doi.org/10.1038/s41566-020-00750-2)
12. S. Abel, F. Eltes, J. E. Ortmann, A. Messner, P. Castera, T. Wagner, D. Urbonas, A. Rosa, A. M. Gutierrez, D. Tulli, P. Ma, B. Baeuerle, A. Josten, W. Heni, D. Caimi, L. Czornomaz, A. A. Demkov, J. Leuthold, P. Sanchis, J. Fompeyrine, Large Pockels effect in micro-

- and nanostructured barium titanate integrated on silicon. *Nat. Mater.* **18**, 42–47 (2019). [doi:10.1038/s41563-018-0208-0](https://doi.org/10.1038/s41563-018-0208-0) [Medline](#)
13. R. R. Subkhangulov, R. Mikhaylovskiy, A. K. Zvezdin, V. Kruglyak, Th. Rasing, A. Kimel, Terahertz modulation of the Faraday rotation by laser pulses via the optical Kerr effect. *Nat. Photonics* **10**, 111–114 (2016). [doi:10.1038/nphoton.2015.249](https://doi.org/10.1038/nphoton.2015.249)
 14. Y. Gao, R. J. Shiue, X. Gan, L. Li, C. Peng, I. Meric, L. Wang, A. Szep, D. Walker Jr., J. Hone, D. Englund, High-speed electro-optic modulator integrated with graphene-boron nitride heterostructure and photonic crystal nanocavity. *Nano Lett.* **15**, 2001–2005 (2015). [doi:10.1021/nl504860z](https://doi.org/10.1021/nl504860z) [Medline](#)
 15. Y.-H. Kuo, Y. K. Lee, Y. Ge, S. Ren, J. E. Roth, T. I. Kamins, D. A. B. Miller, J. S. Harris, Strong quantum-confined Stark effect in germanium quantum-well structures on silicon. *Nature* **437**, 1334–1336 (2005). [doi:10.1038/nature04204](https://doi.org/10.1038/nature04204) [Medline](#)
 16. A. J. Sternbach, S. H. Chae, S. Latini, A. A. Rikhter, Y. Shao, B. Li, D. Rhodes, B. Kim, P. J. Schuck, X. Xu, X.-Y. Zhu, R. D. Averitt, J. Hone, M. M. Fogler, A. Rubio, D. N. Basov, Programmable hyperbolic polaritons in van der Waals semiconductors. *Science* **371**, 617–620 (2021). [doi:10.1126/science.abe9163](https://doi.org/10.1126/science.abe9163) [Medline](#)
 17. A. Chernikov, A. M. van der Zande, H. M. Hill, A. F. Rigosi, A. Velauthapillai, J. Hone, T. F. Heinz, Electrical tuning of exciton binding energies in monolayer WS₂. *Phys. Rev. Lett.* **115**, 126802 (2015). [doi:10.1103/PhysRevLett.115.126802](https://doi.org/10.1103/PhysRevLett.115.126802) [Medline](#)
 18. J. S. Ross, S. Wu, H. Yu, N. J. Ghimire, A. M. Jones, G. Aivazian, J. Yan, D. G. Mandrus, D. Xiao, W. Yao, X. Xu, Electrical control of neutral and charged excitons in a monolayer semiconductor. *Nat. Commun.* **4**, 1474 (2013). [doi:10.1038/ncomms2498](https://doi.org/10.1038/ncomms2498) [Medline](#)
 19. S. Gao, Y. Liang, C. D. Spataru, L. Yang, Dynamical excitonic effects in doped two-dimensional semiconductors. *Nano Lett.* **16**, 5568–5573 (2016). [doi:10.1021/acs.nanolett.6b02118](https://doi.org/10.1021/acs.nanolett.6b02118) [Medline](#)
 20. I. Datta, S. H. Chae, G. R. Bhatt, M. A. Tadayon, B. Li, Y. Yu, C. Park, J. Park, L. Cao, D. N. Basov, J. Hone, M. Lipson, Low-loss composite photonic platform based on 2D semiconductor monolayers. *Nat. Photonics* **14**, 256–262 (2020). [doi:10.1038/s41566-020-0590-4](https://doi.org/10.1038/s41566-020-0590-4)
 21. J. van de Groep, J. H. Song, U. Celano, Q. Li, P. G. Kik, M. L. Brongersma, Exciton resonance tuning of an atomically thin lens. *Nat. Photonics* **14**, 426–430 (2020). [doi:10.1038/s41566-020-0624-y](https://doi.org/10.1038/s41566-020-0624-y)
 22. X. Ling, H. Wang, S. Huang, F. Xia, M. S. Dresselhaus, The renaissance of black phosphorus. *Proc. Natl. Acad. Sci. U.S.A.* **112**, 4523–4530 (2015). [doi:10.1073/pnas.1416581112](https://doi.org/10.1073/pnas.1416581112) [Medline](#)
 23. G. Zhang, S. Huang, A. Chaves, C. Song, V. O. Özçelik, T. Low, H. Yan, Infrared fingerprints of few-layer black phosphorus. *Nat. Commun.* **8**, 14071 (2017). [doi:10.1038/ncomms14071](https://doi.org/10.1038/ncomms14071) [Medline](#)
 24. G. Zhang, A. Chaves, S. Huang, F. Wang, Q. Xing, T. Low, H. Yan, Determination of layer-dependent exciton binding energies in few-layer black phosphorus. *Sci. Adv.* **4**, eaap9977 (2018). [doi:10.1126/sciadv.aap9977](https://doi.org/10.1126/sciadv.aap9977) [Medline](#)

25. W. S. Whitney, M. C. Sherrott, D. Jariwala, W. H. Lin, H. A. Bechtel, G. R. Rossman, H. A. Atwater, Field effect optoelectronic modulation of quantum-confined carriers in black phosphorus. *Nano Lett.* **17**, 78–84 (2017). [doi:10.1021/acs.nanolett.6b03362](https://doi.org/10.1021/acs.nanolett.6b03362) [Medline](#)
26. S. Biswas, W. S. Whitney, M. Y. Grajower, K. Watanabe, T. Taniguchi, H. A. Bechtel, G. R. Rossman, H. A. Atwater, Tunable intraband optical conductivity and polarization-dependent epsilon-near-zero behavior in black phosphorus. *Sci. Adv.* **7**, eabd4623 (2021). [doi:10.1126/sciadv.abd4623](https://doi.org/10.1126/sciadv.abd4623) [Medline](#)
27. C. Chen, X. Lu, B. Deng, X. Chen, Q. Guo, C. Li, C. Ma, S. Yuan, E. Sung, K. Watanabe, T. Taniguchi, L. Yang, F. Xia, Widely tunable mid-infrared light emission in thin-film black phosphorus. *Sci. Adv.* **6**, eaay6134 (2020). [doi:10.1126/sciadv.aay6134](https://doi.org/10.1126/sciadv.aay6134) [Medline](#)
28. Y. Liu, Z. Qiu, A. Carvalho, Y. Bao, H. Xu, S. J. R. Tan, W. Liu, A. H. Castro Neto, K. P. Loh, J. Lu, Gate-tunable giant stark effect in few-layer black phosphorus. *Nano Lett.* **17**, 1970–1977 (2017). [doi:10.1021/acs.nanolett.6b05381](https://doi.org/10.1021/acs.nanolett.6b05381) [Medline](#)
29. The materials and methods are available as supplementary materials.
30. A. Raja, L. Waldecker, J. Zipfel, Y. Cho, S. Brem, J. D. Ziegler, M. Kulig, T. Taniguchi, K. Watanabe, E. Malic, T. F. Heinz, T. C. Berkelbach, A. Chernikov, Dielectric disorder in two-dimensional materials. *Nat. Nanotechnol.* **14**, 832–837 (2019). [doi:10.1038/s41565-019-0520-0](https://doi.org/10.1038/s41565-019-0520-0) [Medline](#)
31. D. Y. Qiu, F. H. da Jornada, S. G. Louie, Environmental screening effects in 2D materials: Renormalization of the bandgap, electronic structure, and optical spectra of few-layer black phosphorus. *Nano Lett.* **17**, 4706–4712 (2017). [doi:10.1021/acs.nanolett.7b01365](https://doi.org/10.1021/acs.nanolett.7b01365) [Medline](#)
32. S. Huang, G. Zhang, F. Fan, C. Song, F. Wang, Q. Xing, C. Wang, H. Wu, H. Yan, Strain-tunable van der Waals interactions in few-layer black phosphorus. *Nat. Commun.* **10**, 2447 (2019). [doi:10.1038/s41467-019-10483-8](https://doi.org/10.1038/s41467-019-10483-8) [Medline](#)
33. D. Çakır, C. Sevik, F. M. Peeters, Significant effect of stacking on the electronic and optical properties of few-layer black phosphorus. *Phys. Rev. B Condens. Matter Mater. Phys.* **92**, 165406 (2015). [doi:10.1103/PhysRevB.92.165406](https://doi.org/10.1103/PhysRevB.92.165406)
34. N. Youngblood, C. Chen, S. J. Koester, M. Li, Waveguide-integrated black phosphorus photodetector with high responsivity and low dark current. *Nat. Photonics* **9**, 247–252 (2015). [doi:10.1038/nphoton.2015.23](https://doi.org/10.1038/nphoton.2015.23)
35. Z. Wu, Y. Lyu, Y. Zhang, R. Ding, B. Zheng, Z. Yang, S. P. Lau, X. H. Chen, J. Hao, Large-scale growth of few-layer two-dimensional black phosphorus. *Nat. Mater.* **20**, 1203–1209 (2021). [Medline](#)